The DOI for this manuscript is doi: 10.1175/MWR-D-17-0095.1

The inner-core temperature structure of Hurricane Edouard (2014): Observations and ensemble variability

Erin B. Munsell[1,2], Fuqing Zhang[3,4], Scott A. Braun[1], Jason A. Sippel[5], and Anthony C. Didlake[3]

[1]Laboratory for Mesoscale Atmospheric Processes, NASA Goddard Space Flight Center, Greenbelt, Maryland

[2]Universities Space Research Association, Columbia, Maryland

[3]Department of Meteorology and Atmospheric Science, The Pennsylvania State University, University Park, Pennsylvania

[4]Center for Advanced Data Assimilation and Predictability Techniques, The Pennsylvania State University, University Park, Pennsylvania

[5]NOAA's Atlantic Oceanographic and Meteorological Laboratory, Hurricane Research Division, Miami, Florida

Submitted to Monthly Weather Review for publication as an article

October 17th, 2017

Corresponding author address: Dr. Erin B. Munsell, Laboratory for Mesoscale Atmospheric Processes, Code 612, NASA Goddard Space Flight Center, Greenbelt, MD 20771. E-mail: erin.b.munsell@nasa.gov

Abstract

The inner-core thermodynamic structure of Hurricane Edouard (2014) is explored, primarily through an examination of both high-altitude dropsondes deployed during NASA's Hurricane and Severe Storm Sentinel (HS3) and a 60-member convection-permitting ensemble initialized with an ensemble Kalman filter. The 7-day forecasts are initialized coincident with Edouard's tropical depression designation and include Edouard's significant intensification to a major hurricane. Ten-member ensemble groups are created based on timing of near rapid intensification (RI) onset, and the associated composite inner-core temperature structures are analyzed.

It is found that at Edouard's peak intensity, in both the observations and the simulations, the maximum inner-core perturbation temperature (~10–12 K) occurs in the mid-levels (~4–8 km). In addition, in all composite groups that significantly intensify, the evolution of the area-averaged inner-core perturbation temperatures indicate that weak to moderate warming (at most 4 K) begins to occur in the low- to mid-levels (~2–6 km) ~24–48 h prior to RI, and this warming significantly strengthens and deepens (up to ~8 km) ~24 h after RI has begun. Despite broad similarities in the evolution of Edouard's warm core in these composites, variability in the height and strength of the maximum perturbation temperature and in the overall development of the inner-core temperature structure are present amongst the members of the composite groups (despite similar intensity time series). This result and concomitant correlation analyses suggest that the strength and height of the maximum perturbation temperature is not a significant causal factor for RI onset in this ensemble. Fluctuations in inner-core temperature structure occur either in tandem with or after significant intensity changes.

1. Introduction

Tropical cyclones (TCs) are frequently distinguished from extratropical cyclones by differences in their vertical structure of temperature and wind. TC vortices are "warm core", which means that the tropospheric temperature within the inner-core of the cyclone is warmer than the surrounding environment. Since the tangential wind fields of TCs are nearly balanced (Willoughby 1990), thermal wind dictates that this negative radial temperature gradient balances tangential winds that are maximized at low-levels and decrease with height. The first observational studies that attempted to determine the radial and vertical temperature structure of TCs analyzed flight-level temperature measurements at multiple altitudes of Hurricanes Cleo (1958; La Seur and Hawkins 1963), Hilda (1964; Hawkins and Rubsam 1968) and Inez (1966; Hawkins and Imbembo 1976). Using the Jordan (1958) mean sounding as a reference profile, these studies concluded that the maximum inner-core perturbation temperature typically occurred between 250–300 hPa, although a secondary maximum near 600–650 hPa was observed in Inez.

Primarily because of these initial observational studies, it became widely accepted that the height of the maximum perturbation temperature (or "warm core") in TCs is typically confined to the upper-troposphere. However, more recent studies have suggested that this may not be the case, with Stern and Nolan (2012) arguing that the inner-core temperature structure in TCs is simply not well known. This conjecture is mainly because, until recently, many of the flights into TCs were performed primarily below 6 km, and the duration of storm sampling was typically ~6 h. Halverson et al. (2006) used dropsondes deployed by NASA's DC-8 (from 11–12 km height) and ER-2 (from 19 km) aircraft on 10 September 2001 into Hurricane Erin and found a maximum perturbation temperature (using an environmental dropsonde as a reference profile) of 11 K near 500 hPa. In addition, Durden (2013) composited high-altitude dropsondes from inner-core soundings of 9 different storms and found that the height of the maximum perturbation temperature existed anywhere between 750 and 250 hPa.

Recent NASA field campaigns, such as the Genesis and Rapid Intensification Processes (GRIP; Braun et al. 2013) and the Hurricane and Severe Storm Sentinel (HS3; Braun et al. 2016) have attempted to address the lack of spatial and temporal sampling through the utilization of high-altitude aircraft. Stern and Zhang (2016) used dropsondes deployed during GRIP by the DC-8 throughout the lifetime of Hurricane Earl (2010) to investigate the evolution of the inner-core temperature structure and whether or not any relationship existed between the height of the maximum perturbation temperature and the intensity evolution. Utilizing an environmental reference temperature profile (measured by dropsondes deployed by NOAA's G-IV aircraft), two distinct perturbation temperature maxima of similar magnitude were constantly observed, one in the mid-troposphere (4–6 km) and the other in the upper-troposphere (9–12 km). In addition, no relationship was found between the height of Earl's maximum perturbation temperature and either the current intensity or subsequent intensity changes. Komaromi and Doyle (2016) examined the composite inner-core temperature structure of 6 different TCs using dropsondes deployed across 16 HS3 missions and also found that neither the height nor the magnitude of the warm core correlated with intensity change.

More recent modeling studies have also suggested that the height of the warm core in TCs may be lower in the troposphere than traditionally believed. Stern and Nolan (2012) and Stern and Zhang (2013a,b) performed an extensive series of idealized experiments in which the microphysics, storm size, magnitude of vertical wind shear, and intensity all varied, and consistently obtained TCs with maximum inner-core temperature perturbations in the mid-levels (4–8 km). Wang and Wang (2014) obtained two distinct maxima in perturbation temperature in their simulation of Supertyphoon Megi (2010), one in the mid-levels (5–6 km) and the other in the upper-levels (15–16 km); however, the upper-level warm core did not form until a period of rapid intensification (RI) began when the storm was already at category 2 strength. In an idealized experiment of a TC in radiative convective equilibrium performed by Ohno and Satoh (2015), the inner-core maximum perturbation temperature was found to be at ~9 km throughout much of the intensification phase, and a secondary upper-level temperature perturbation only developed once the TC reached near-major hurricane strength. Finally, in a simulation of Hurricane Earl, Chen and Gopalakrishnan (2015) found that the maximum perturbation temperature occurred at a height of 8 km at peak intensity.

As discussed above, a majority of recent modeling studies have suggested the presence of a mid-level maximum perturbation temperature in the inner-core of TCs. In contrast, in simulations of Hurricane Wilma (2005) performed by Chen et al. (2011) and Chen and Zhang (2013), a single maximum perturbation temperature was found at 14 km. It was also argued that the formation of this temperature perturbation at this height helped trigger Wilma's significant period of RI. This hypothesis will be explored in the case of Hurricane Edouard's (2014) near-RI[1] event in this study through the use of high-altitude dropsondes, additional HS3 and satellite observations, and a convection-permitting 60-member ensemble simulation.

Hurricane Edouard was a named-tropical cyclone from 11–19 September 2014 that remained over the open Atlantic Ocean throughout its lifetime (Stewart 2014). The tropical wave that eventually became Edouard exited the African coast on 6 September. As the broad area of low-pressure tracked westward, convection increased near the center of the surface low, causing

[1] Although Edouard did not officially undergo RI (according to the NHC criteria), the period of intensification was significant (a "near-RI event"). Therefore, RI timing is examined in this ensemble as it is traditionally defined, because it is more straightforward to do so.

the wave to be designated as a tropical depression at 1200 UTC 11 September. Steady intensification followed, and Edouard became a tropical storm early on 12 September and a hurricane early on 14 September. Over the next 24 h, a period of significant intensification occurred (12.9 m s^{-1} or 25 kts), and by 1200 UTC 16 September, Edouard reached its peak intensity with winds of 54.0 m s^{-1} (105 kts). Edouard began to weaken almost immediately thereafter as an eyewall replacement cycle (ERC) occurred, and as Edouard turned northward and northeastward, it accelerated ahead of an approaching mid-latitude trough. On 18 September, Edouard turned eastward and rapidly weakened to a tropical storm as it became embedded in strong vertical wind shear associated with the mid-latitude westerlies. It was subsequently reclassified as a strong post-tropical cyclone early on 19 September.

In addition to undergoing a period of significant intensification, Edouard was also notable for the numerous research missions conducted at times simultaneously throughout its lifetime (Stewart 2014). The NOAA WP-3D Hurricane Hunters conducted eight missions between 11–19 September, while NASA's Global Hawk performed four missions into and around Edouard throughout its lifetime, sampling the TC for up to 18 consecutive hours during each mission, as part of the 2014 campaign of HS3. In addition, the Global Hawk dropsondes were released from altitudes greater than 18 km, which yielded some of the first high-resolution samples of inner-core TC temperature structure throughout the troposphere and lower stratosphere.

The overall goal of this study is to investigate the evolution of the inner-core temperature structure of Edouard prior to and throughout its period of significant intensification by using both the unusual variety of observations and a 60-member convection-permitting ensemble simulation generated by the Pennsylvania State University (PSU) Real-time Atlantic Hurricane Analysis and Forecast System. In particular, the ensemble simulation provides an opportunity to not only thoroughly examine the evolution of the modeled inner-core temperature structure, but also to examine the variability of the height and strength of the maximum temperature perturbation for groups of members that have similar intensity evolutions yet a variety of RI-onset times throughout the simulation.

Section 2 provides a description of the PSU real-time hurricane forecast and analysis setup and the available observations of Edouard’s inner-core temperature structure. Section 3 presents an evaluation of Edouard’s observed and simulated inner-core temperature structure, as well as correlation analyses that examine the ensemble variability of Edouard’s warm core throughout the period of significant intensification. Finally, section 4 summarizes the main conclusions of this study.

2. Methodology and data

2.1 PSU WRF-EnKF real-time Atlantic hurricane analysis and forecast system

The 60-member ensemble simulation utilized in this study was originally a 126-h forecast initialized at 1200 UTC 11 September by the PSU real-time Atlantic hurricane analysis and forecast system (Zhang et al. 2009, 2011; Zhang and Weng 2015; Weng and Zhang 2016). For the 2014 configuration of this system, version 3.5.1 of the Advanced Research version of the Weather Research and Forecasting model (ARW-WRF; Skamarock et al. 2008) is coupled with an ensemble Kalman filter (EnKF) algorithm for data assimilation. Observations that are assimilated when available include Global Telecommunication System (GTS) conventional and reconnaissance data, superobservations generated from the airborne tail Doppler radar (TDR) on the NOAA P-3 aircraft (Weng and Zhang 2012), satellite-derived winds (Weng and Zhang 2016), and dropsondes deployed from the NOAA/National Center for Atmospheric Research (NCAR) Advanced Vertical Atmospheric Profiling System (AVAPS) collected during HS3 flights (Braun et al. 2016). Three two-way nested domains are utilized with horizontal grid spacings of 27, 9, and 3 km, and all domains have 43 vertical levels and a model top at 10 hPa. The outermost domain is fixed, while the inner domains follow the vortex of the TC of interest. All physics configurations in WRF are the same as in Munsell et al. (2017).

The PSU WRF-EnKF system was first initialized for the invest area that eventually became Edouard at 0000 UTC 4 September, utilizing Global Forecast System (GFS) analyses. The first data assimilation cycle was performed on all three domains 12 h into integration, and continuous cycling occurred at 3 h intervals thereafter. The initial and lateral boundary conditions for the ensemble were generated by adding perturbations derived from the background error covariance of the WRF variational data assimilation system (Barker et al. 2004). In addition, in order to examine Edouard's inner-core temperature structure throughout its period of strong intensity, 40 of the 60 ensemble members (those that comprised the composite groups in Munsell et al. 2017; detailed below) were extended an additional 42-h through 1200 UTC 18 September, resulting in a 168-h forecast initialized at 1200 UTC 11 September.

2.2 Observations of Hurricane Edouard's inner-core temperature structure

During the 2014 campaign of HS3, four flights utilizing NASA's Global Hawk were performed throughout the lifetime of Hurricane Edouard. These flights spanned Edouard's evolution from a newly formed tropical storm (11–12 September), the significant period of intensification to a strong category 2 TC (14–15 September), Edouard's maintenance near peak intensity (16–17 September), and Edouard's rapid weakening as it began to transition to an extratropical cyclone (18–19 September; Braun et al. 2016). The first two Edouard flights occurred during the original 5-day simulation window (15–27 h and 72–93 h), while the third flight was performed within the 42-h extension of part of the ensemble forecast (123–141 h).

Observations collected during the third HS3 flight, including 87 AVAPS dropsondes (Wick 2015) deployed from ~18 km and data from the University of Wisconsin's Scanning High-Resolution Interferometer Sounder (S-HIS; Revercomb 2015), contain information about the inner-core temperature structure of Edouard. The dropsondes have been quality controlled and postprocessed at the NCAR Earth Observing Laboratory (EOL) using NCAR's Atmospheric Sounding Processing Environment (ASPEN) software (Young et al. 2014). None of the HS3 observations were assimilated in the ensemble forecast analyzed in this study, as they were not available at the time of initialization.

Eight flights from two NOAA P-3 and a G-IV aircraft were also performed throughout Edouard's lifetime between 12 and 17 September as part of the NOAA Intensity Forecasting Experiment (IFEX; Rogers et al. 2013a). This study utilizes data collected by the TDR to analyze Edouard's wind field and overall structure; dropsondes deployed by the P-3 and G-IV are not utilized to examine the inner-core temperature structure because of the P-3's significantly lower deployment altitude and the G-IV's focus on the sampling of the TC's environment.

3. Results and Discussion

3.1 PSU WRF-EnKF ensemble track and intensity evolution

As the primary goal of this study is to examine the evolution of the inner-core temperature structure of Edouard throughout the period of significant intensification, the 126-h forecast chosen for analysis encompasses the TC's designation as a tropical depression through peak intensity (1200 UTC 11 September–1800 UTC 16 September). This ensemble is identical to that investigated extensively in Munsell et al. (2017), which examined the predictability and dynamics associated with the variability in RI-onset times within the ensemble. This ensemble was also used to study various other aspects of the dynamics and predictability of Edouard (Tang and Zhang 2016; Tang et al. 2017; Melhauser et al. 2017; Fang et al. 2017). Figure 1a shows the National Hurricane Center's (NHC) Best Track for Hurricane Edouard, as well as the deterministic (APSU) and ensemble members for the PSU WRF-EnKF forecast, while Figs. 1b and 1c present the corresponding evolution of the minimum sea level pressure (SLP; in hPa) and maximum 10-m wind speed (in kt). Overall, the deterministic track and intensity forecast closely follows that of the Best Track, and a substantial number of members (~25) predict an RI-onset time and rate of intensification comparable to the Best Track. A majority of the remaining members intensify at a similar rate as the Best Track; however, variability of up to 48–60 h in the timing of RI onset is present, with some members not intensifying at all in the 126-h forecast.

As in past ensemble sensitivity studies (e.g. Munsell et al. 2013, 2015, 2017; Munsell and Zhang 2014; Rios-Berrios et al. 2015), 10-member composite groups are created according to their timing of intensification to examine the variability of the development of the inner-core temperature structure. These composite groups are identical to those in Munsell et al. (2017): GOOD contains members whose RI-onset times are approximately that of the Best Track (1200 UTC 14 September, or 72 h), GOOD_EARLY (GOOD_LATE) members undergo RI 24 h prior to (after) Best Track RI, and POOR members do not intensify substantially in the 126-h simulation window. To encompass the entirety of Edouard's peak intensity and the HS3 flight on 16–17 September (as indicated on Figs. 1b and 1c), the 40 members that comprise these composite groups have been extended to 1200 UTC 18 September, and the resulting 168-h forecasts of track, minimum SLP, and maximum 10-m wind speed are plotted on Fig. 1. Towards the end of this new simulation window, the members of the developing composites have begun to weaken (although not as significantly as in the Best Track) as Edouard turns towards the northeast and into less favorable environmental conditions. However, the slower and more westward positions of the POOR members lead to some intensification after 144 h. Much of the analysis in this study of the ensemble variability of the inner-core temperature structure evolution utilizes these composite groups, and the forecasts of the remaining 20 ensemble members (Other in Fig. 1) were not extended. Though the evolution of the majority (15) of the "Other" members resembles that of the GOOD members, the cumulative root-mean square intensity errors are larger than in the GOOD members. The remaining 5 "Other" members do not significantly intensify, as in POOR.

3.2 Comparison of PSU WRF-EnKF wind field to observations

Before analyzing the observed and modeled inner-core temperature structure of Edouard in greater detail, it is useful to compare the observed horizontal and tangential wind fields to the ensemble since the structure of the tangential winds is closely related to the inner-core temperature structure through thermal wind balance. Figures 2 and 3 show storm-centered horizontal cross sections of composite 2-km wind speed and azimuthally-averaged vertical cross-sections of tangential wind collected by the TDRs on the two NOAA P-3 aircraft on 14, 15, and 16 September (Figs. 2a-c and 3a-c; flight times indicated on Figs. 1b and 1c), and the corresponding GOOD (Figs. 2d-f and 3d-f) and GOOD_LATE (Figs. 2g-i and 3g-i) composites from the WRF-EnKF forecast. For the TDR data, NOAA's Hurricane Research Division (HRD) performs a three-dimensional analysis of the Cartesian horizontal and vertical velocities by using the automated technique of Gamache et al. (2004). These 5-km analyses have been composited across the various legs of each ~3-h flight pattern. The observational composites in Fig. 2 are somewhat comparable to those in Rogers et al. (2016) as they utilize the same P-3 data; however, Rogers et al. (2016) uses a finer grid spacing of 2-km and their composites are storm-relative, while the Fig. 2 composites are ground-relative. The 2-km winds as measured by the dropsondes deployed during the third HS3 flight (16–17 September) are also indicated on Fig. 2c.

The 14 September P3 flight occurred near the beginning of Edouard's intensification from a tropical storm to a strong category-2 hurricane. The P3 data (Fig. 2a) show that Edouard was somewhat asymmetric at this time, with the maximum 2-km winds of ~40 m s^{-1} located to the north of the surface center. The surface radius of maximum winds (RMW) was ~25 km, while 30 m s^{-1} winds extended upwards through a height of ~8 km in this region (Fig. 3a). The GOOD composite at this time (Fig. 2d) simulates most of the same characteristics, though the simulated vortex is slightly more asymmetric with the maximum 2-km winds (~36 m s^{-1}) located northeast of the surface center. In addition, the GOOD composite vortex has a larger RMW of ~40 km, and the vortex is slightly weaker and shallower with 30 m s^{-1} wind up to only ~5 km (Fig. 3d). It is evident in the composites from 15 September that the period of intensification was well underway, as both the P3 data (Figs. 2b and 3b) and the GOOD composite (Figs. 2e and 3e) have maximum 2-km winds of ~55 m s^{-1}, near-surface winds of ~48 m s^{-1}, an expanded RMW (~40 km) that noticeably slopes outward with height, and a deep vertical extent of 30 m s^{-1} winds (~10–11 km).

Despite general agreement between the P3 data and the GOOD composites on 14 and 15 September, the composites are markedly different from the radar analyses on 16 September. The P3 data and the dropsondes deployed during the 16–17 September HS3 flight (Fig. 2c) indicate that the vortex at 2 km weakened to ~45 m s^{-1}, with the strongest winds located to the southeast of the surface center. A secondary wind maximum is also apparent in the observations ~50 km east of the center, as an ERC was occurring throughout these flights. However, the GOOD composite (Fig. 2f) shows a stronger (~60 m s^{-1}) and more symmetric vortex with no evidence of a secondary wind maximum. The vertical cross section of P3 tangential wind data (Fig. 3c) indicates that Edouard's near-surface winds (~0.5 km) decreased somewhat to ~44 m s^{-1}, and the RMW contracted to 30 km and became more upright with height. Conversely, the near-surface winds of the GOOD composite vortex are significantly stronger (upwards of 60 m s^{-1}), the RMW remains at 40 km, and the outward slope of the RMW has increased (Fig. 3f).

Though there is considerable disagreement between the observed and simulated composites on 16-17 September, the simulation results can still provide useful insights at this time. The disagreement results from the failure of some GOOD members to capture an ERC and also a tendency of GOOD to decay at a slower rate than observed. The GOOD_LATE composites at this time are in better agreement with the observed composites, as the minimum SLP (Fig. 1b), horizontal 2-km winds (Fig. 2i), 0.5-km tangential winds, and the RMW (Fig. 3i) are comparable. However, due to their later RI onsets, the GOOD_LATE members reach their peak intensities just prior to this time. Despite the lack of any secondary wind maxima in the composites, a closer examination of the evolution of the 1-km tangential winds and vertical velocities reveals that a majority (14 out of 20) of the GOOD and GOOD_LATE members show evidence of an ERC (not shown). Therefore, although neither the GOOD nor GOOD_LATE members simulate the exact structural evolution of Edouard, both composite groups are able to accurately capture RI, and many members replicate the ERC in the decay phase. This allows for reasonable comparisons to the observed inner-core temperature structure.

3.3 Analysis of the observed warm core

The inner-core temperature structure of Edouard was only sufficiently sampled for further analysis throughout the 16–17 September flight, when Edouard was a strong category 2 storm. During this period, 87 dropsondes were deployed, with 21 of them passing within 50 km of the surface center[2] at some point during their descent. The positions of these inner-core dropsondes, color-coded by distance from Edouard's surface center, are shown in Fig. 4a. It should be noted that only 6 of these dropsondes are confined to within 20 km of Edouard's surface center throughout descent, which can lead to an underestimation of the magnitude of the inner-core perturbation temperature.

The vertical profiles of wind speed as measured by the 16–17 September inner-core dropsondes are shown in Fig. 4b. About one-third of the inner-core dropsondes have wind speeds less than 20 m s^{-1} throughout their vertical profile, indicating that these dropsondes likely remained within the eye of Edouard for the majority of their descent. Vertical profiles of equivalent potential temperature (θ_e in K; Fig. 4c) confirm that these inner-core dropsondes primarily remained within Edouard's eye, as higher values of θ_e are present throughout the profiles, peaking at 370–375 K near the surface. The remainder of the inner-core dropsondes measured wind speeds in excess of 30–45 m s^{-1}, particularly at low-levels, and therefore likely sampled at least part of Edouard's eyewall. These dropsondes also have cooler θ_e profiles throughout most of the troposphere, again suggesting that they remained mostly in the eyewall throughout descent.

In order to calculate vertical profiles of perturbation temperature, a reference profile must first be selected. Stern and Nolan (2012) extensively discussed the various choices of reference profile; most observational and modeling studies either use a mean climatological sounding, such as the Jordan (1958) or the Dunion (2011) moist tropical sounding, or a near-storm environmental profile calculated using available observational or numerical data within a

[2] The estimated storm centers are obtained from S-HIS data collected during the 9 eye overpasses that the Global Hawk executed during the 16–17 September flight. These center fixes were subsequently interpolated to 2-min intervals, and the appropriate center was chosen based on the time that the dropsonde was deployed.

specified range of distance from the surface center of the TC of interest. Durden (2013) explored the impacts of using a mean climatological (Dunion) versus a near-storm environmental reference profile and found that the resulting perturbation temperature structures were at higher altitudes and had larger magnitudes in perturbation temperature when a climatological sounding, such as Dunion (2011), was used. The Hurricane Earl perturbation temperatures calculated by Stern and Zhang (2016), in which comparisons were also made for multiple reference profiles (the Dunion sounding versus environmental profiles), were consistent with the Durden (2013) results. Therefore, this study utilizes an environmental profile as in Stern and Zhang (2016), in which the reference profile is calculated from either observations or numerical data between 300 and 700 km from Edouard's surface center.

Given this near-storm environmental reference profile, the resulting perturbation temperatures as measured by the inner-core dropsondes deployed throughout the 16–17 September HS3 flight are shown in Fig. 4d. From these profiles (again color-coded by the distance from Edouard's surface center), it is clear that the perturbation temperature magnitudes noticeably increase inwards. In addition, there appear to be two distinct shapes of perturbation temperature profiles that also have a dependence on distance. Most of the dropsondes that were deployed closer to Edouard's surface center (within 20-km of the surface center; Fig. 5) have two distinct perturbation temperature maxima, one between 4 and 6 km and the other between 7 and 9 km (Figs. 5a, 5c, and 5f). Both of these near-center perturbation temperature maxima are of similar strength, ~10–12 K. A few of these dropsondes also have a third maxima of similar strength near ~10 km (Figs. 5e and 5g). However, the majority of the dropsondes closer to Edouard's RMW (~30 km) have only one maximum in perturbation temperature, predominantly between heights of 7 and 9 km. Furthermore, this single perturbation temperature maximum (~7–

9 K) is weaker than the perturbation temperature maxima that are closer to the surface center, consistent with Zawislak et al. (2016). Regardless of distance from the TC surface center, nearly all inner-core dropsondes measure decreasing perturbation temperatures above 10 km, and there is no evidence of upper-tropospheric maxima in perturbation temperature through heights of 18 km.

In addition to the dropsondes released on 16–17 September, additional observations of Edouard's inner-core temperature structure were obtained from the airborne S-HIS and the spaceborne Advanced Microwave Sounding Unit (AMSU-A). Figure 6 shows a radius-height cross section of the azimuthally averaged composite inner-core perturbation temperature for Edouard for these observational sources and the GOOD_LATE members from the WRF-EnKF ensemble. All composites in Fig. 6 are calculated using the GOOD_LATE environmental reference profile averaged over a 300–700 km annulus centered on the surface center, with the exception of the AMSU-A data (Fig. 6d). The dropsonde perturbation temperatures discussed above (Fig. 4) are replotted using the modeled reference profile in Fig. 6b; similar conclusions can be drawn as from the individual vertical profiles of perturbation temperature (Fig. 4d). Two perturbation temperature maxima of ~10 K are present in the near center region (between 10 and 20 km), while the third perturbation temperature maxima at a height of ~10 km that was observed in some of the near center dropsondes also is seen. At and just outside the eyewall (~40–60 km from the surface center), a single weaker maximum in perturbation temperature is evident.

The azimuthal-mean perturbation temperature composite for the S-HIS data is shown in Fig. 6c. It should be noted that the capability of the S-HIS to sample the warm core is limited since this instrument cannot "see" through clouds. Within the eye region, however, where the cloud cover is reduced, a region of relatively strong (~10–11 K) perturbation temperatures is sampled between heights of 7 and 10 km within radii of up to 25 km. Therefore, the overall structure of the inner-core temperature appears to be similar between the S-HIS and dropsonde data for the 16–17 September HS3 flight, with the S-HIS analysis slightly cooler than the perturbation temperature maxima measured by the dropsondes.

In addition to direct measurements of Edouard's inner-core temperature structure, remote-sensing instruments on satellites also have some skill in resolving the warm core of TCs (Knaff et al. 2004); however, the lack of resolution in both the horizontal (~50 km) and vertical (6 usable channels) limits them (Stern and Nolan 2009). Figure 6d shows the azimuthal-mean perturbation temperature composite of Edouard's inner-core as measured by the AMSU-A multi-channel microwave temperature sounder at 2025 UTC 16 September. The satellite data has been processed by the University of Wisconsin's Cooperative Institute for Meteorological Satellite Studies (UW-CIMSS); the environmental reference profile used to calculate perturbation temperatures is created from temperature retrievals at various points around the TC that are ~500 km from the surface center. The composite perturbation temperature structure reveals two distinct maxima in perturbation temperature, one slightly higher in the atmosphere (~9–11 km) than in either the dropsonde or S-HIS data, and one significantly lower in the atmosphere (near the surface). In addition, the magnitudes of these maxima are much weaker (~4 K for the upper maximum and ~6 K for the near-surface maximum). This incongruent inner-core perturbation temperature structure almost certainly results from the lack of horizontal and vertical resolution in the AMSU-A data; the 6 channels (4–9) utilized to construct this composite perform temperature retrievals at horizontal resolution of 48 km at nadir and have weighting functions that are maximized at heights of ~1, 5, 10, 12, 15, and 17.5 km, respectively. Based on this composite, it is clear that the AMSU-A temperature retrievals are inadequate for observing the inner-core temperature structure of Edouard.

3.4 Analysis of the simulated warm core: Comparison to observations

Although both the horizontal and tangential wind composite comparisons between the P3 data and the WRF-EnKF ensemble were mostly favorable (Figs. 2 and 3), Edouard's simulated inner-core temperature structure should also be verified before more in-depth analysis is performed. Figure 6a shows the azimuthal-mean vertical cross section of perturbation temperature for the GOOD_LATE members at 0000 UTC 17 September, which coincides with the approximate midpoint of the 16–17 September HS3 flight. The height of the maximum perturbation temperature in the eye region in the GOOD_LATE composite is ~6 km, which agrees fairly well with the height of the lowest perturbation temperature maximum in the dropsondes. However, unlike in the innermost dropsondes, there is only one distinct maximum in perturbation temperature in the eye, the radial extent of this maximum (perturbations of at least 8 K) is only ~30 km, and the vertical extent of these perturbations is confined to below 9 km.

The overall vertical structure of composite GOOD_LATE inner-core temperature is somewhat consistent with the dropsonde data, as the region of the most significant perturbation temperatures (at least 7 K) extends upwards from a height of ~4 km and the strength of the maximum in temperature perturbation is ~10–12 K in both composites (Figs. 6a and 6b). To more quantitatively compare the inner-core temperature structure of GOOD_LATE and the dropsondes, perturbation temperatures averaged within a 50-km radius and over various altitude ranges are calculated throughout the period of the HS3 flight (Figs. 7a–7c). At the beginning of the HS3 flight (~1500 UTC 16 September; 123 h), the observed inner-core perturbation temperatures were warmer (~4 K) than in the GOOD_LATE composite in all three layers.

However, by 6 h into the flight (~2100 UTC 16 September; 129 h) as Edouard began to weaken, the dropsondes and the GOOD_LATE members are in better agreement (primarily within a standard deviation of each other) and remain so for the remainder of the flight, with layer-averaged inner-core perturbation temperatures of ~6–7 K in the low- to mid-levels (4–6 km) and ~7–9 K in the mid- to upper-levels (6–8 km and 8–10 km).

A scatterplot of the height of the temperature maximum as a function of radius for dropsondes and the GOOD_LATE composite (Fig. 7d) expands upon the comparisons of the strength of the maximum inner-core perturbation temperature in the selected layers. The maximum perturbation temperature in the GOOD_LATE composite within a 10-km radius is ~10 K at a height of 6 km, while the dropsondes measured a slightly stronger and higher maximum perturbation temperature (~11–12 K at a height of ~8 km). The height of the temperature maximum increases with radius, while the strength decreases in both the dropsondes and the GOOD_LATE composite. Although the temperature-maxima heights are in agreement between the two datasets at all radii outwards of 10 km, the GOOD_LATE perturbation temperature maxima are ~2–3 K cooler than those measured by the dropsondes. Despite some minor discrepancies, the available observations of Edouard's inner-core temperature structure obtained throughout the 16–17 September HS3 flight compare favorably with the GOOD_LATE composite, which allows for additional analysis of the development of the warm core within the WRF-EnKF ensemble.

3.5 Analysis of the simulated warm core: Relationship to RI

The 10-member composite groups from the WRF-EnKF ensemble are now utilized to explore the relationship between Edouard's inner-core temperature structure and RI-onset time. Figure 8 shows radius-height cross sections of azimuthal-mean perturbation temperature for the

GOOD_EARLY (Fig. 8a), GOOD (Fig. 8b), GOOD_LATE (Fig. 8c), and POOR (Fig. 8d) composite groups at 0000 UTC 17 September (132 h), which coincides with the midpoint of the HS3 flight just after Edouard's peak intensity. GOOD_EARLY and GOOD members had respectively completed their intensification about 24 and 12 hours before this time, and the two composites have fairly similar perturbation temperature structures. A distinct and relatively strong maximum in perturbation temperature of ~10 K is present in the mid-levels in both composites, although this maximum is slightly higher (~7 km rather than ~6 km), and the radial extent of the 10 K contour is slightly larger in GOOD_EARLY (~20 km rather than ~10 km).

As the other composites differ in evolutionary stages, more discrepancy exists in their inner-core temperature structures at this time. At 132 h, the GOOD_LATE members have just reached their peak intensities but are ~15 kts weaker than the GOOD_EARLY or GOOD members at their peak intensities (Fig. 1c). This difference is reflected in the perturbation temperature structures; the magnitude of the warm core is ~1.5 K cooler in GOOD_LATE, and the region of most significant perturbation temperature (at least ~8 K) does not extend upwards as high (~8.5 km as opposed to ~10.5 km). In addition, the warming is not as deep, as perturbation temperatures exceeding 4 K do not extend above 12 km (Fig. 8c). Finally, although some of the POOR members begin to intensify towards the end of the 7-day simulation window, these late-developing members have only just begun intensification at 132 h, and a developing warm core at ~7 km of ~4 K is present (Fig. 8d).

Additional insight on warm-core evolution can be derived from the availability of WRF-EnKF ensemble output across the simulation window. Figure 9 shows the 7-day evolution of the inner-core area-averaged (within a radius of 25-km) perturbation temperature vertical structure for the four composite groups. For the developing composites (GOOD_EARLY, GOOD, and

GOOD_LATE), the RI-onset times of the respective composites are also indicated; the POOR members do not significantly intensify in the simulation window. All composite groups initially have weak mid-level inner-core perturbation temperatures (< 2 K), as the members are only of tropical depression or weak tropical storm strength and substantial warming has not yet occurred throughout the vortex. In the GOOD_EARLY and GOOD composites (Figs. 9a and 9b), some warming (average perturbation temperatures of ~3 K) is evident ~24 h prior to RI onset in the low- to mid-levels (~4–6 km). In the GOOD_LATE composite (Fig. 9c), a similar pattern of warming begins up to 48 h prior to RI onset (~48 h; as in GOOD); however, onset of RI is not imminent and the moderate warming is confined to below 6 km until just prior to RI (~96 h).

Approximately 3–6 h prior to RI in all three developing composites (Figs. 9a–c), a region of moderate warming (perturbation temperatures of at most 4 K) extends upwards through 8–10 km. Rapid deep-layer warming occurs as the RI process begins. This signal occurs approximately in tandem with the intensification process, suggesting that this upper-level warming is not a trigger of RI; this possibility will be explored in more detail below. As intensification proceeds in the GOOD_EARLY, GOOD, and GOOD_LATE composites, warming occurs throughout most of the vortex (~2–10 km) over the first 24 h of RI, with maximum perturbation temperatures of ~7 K present in the mid-levels (6–8 km).

By 48–72 h after RI onset has begun in the developing composites, the overall maximum temperature perturbation (~9–11 K) has developed at a height of ~7–8 km. The maximum temperature perturbation in each of the composites has not only increased in magnitude over time, but the height of the maximum warming has also steadily increased from ~3–5 km prior to RI-onset upwards to ~7–8 km after intensification. Throughout this period, as Edouard is steadily intensifying, warming has become more prevalent throughout the entirety of the vertical column, with perturbation temperatures of at least ~4 K approaching 14–16 km in GOOD_EARLY and GOOD. However, this upper-level warming is likely a consequence of the significant intensification that Edouard is undergoing throughout this period, as these perturbation temperatures do not develop at these heights until 24–48 h after RI onset.

Throughout the 7-day simulation window, significant inner-core perturbation temperatures do not develop in POOR (Fig. 9d), as significant intensification does not occur in these members. A developing warm core becomes apparent in the last 24 h of the simulation (144–168 h), as about half of the POOR members begin intensifying (Figs. 1b and 1c). However, the intensification is in its early stages, and the simulation would need to be further extended to examine the perturbation temperature structure evolution in more detail.

3.6 Analysis of the simulated warm core: Ensemble composite group variability

The WRF-EnKF ensemble also allows for the analysis of the variability of the development of Edouard's warm core for ensemble members that have a very similar intensity evolution (e.g. within the composite groups). Figure 10 shows radius-height cross sections of azimuthal-mean temperature perturbation for 9 randomly chosen members (out of 10 for ease of presentation) of the GOOD composite group just after peak intensity (0000 UTC 17 September). The inner-core temperature structures of the individual GOOD members have some broad similarities to the GOOD composite temperature structure at this time (Fig. 8b). The maximum inner-core temperature perturbations are located in the mid-levels (primarily ~6 km), while perturbations of at least 8 K extend ~20 km radially outwards in the vicinity of the maximum.

However, variability in the precise height and strength of the maximum temperature perturbations across the members is notably present. For example, within the temperature structures of the 9 members, the height of the maximum perturbation temperature can occur as low as 5 km (Figs. 10b, 10e, and 10h) or as high as 9 km (Fig. 10g), while the strength of this maximum varies from as weak as 9 K (Fig. 10g) to as strong as 12 K (Figs. 10a and 10b). It should also be noted that none of the members have upper-level (>10 km) perturbation temperature maxima, as has been seen in numerous previous modeling studies. In addition, at the height of the perturbation temperature maxima, the radial extent of the most significant warming does not vary as substantially. However, throughout the profile perturbation temperatures of at least 7.5 K can at times be confined to within 25 km of the surface center (Fig. 10e), but they can also extend as much as 40 km outwards (Figs. 10b, 10h, and 10i).

Figure 11 shows the evolution of the area-averaged (within 25 km radius) perturbation temperature vertical structure for the same 9 randomly chosen GOOD members whose radius-height cross-sections of perturbation temperature are in Fig. 10. The storms in these members undergo slow, yet steady intensification over the first 72 h before a period of RI begins, coincident with the Best Track RI onset (Figs. 1b and 1c). Variations in the exact timing of RI onset across the members of the GOOD composite group are limited to 6 h or less; therefore, the composite RI-onset time is indicated on all panels in Fig. 11. As in the comparisons between the radius-height cross sections of perturbation temperature, the evolution of both the composite (Fig. 9b) and the individual members of GOOD share some general characteristics. Little to no warming is present over the first 24 h throughout the vertical column, as the members do not strengthen appreciably over this period. In addition, as RI onset is approached between 24–72 h, evidence of moderate warming exists in most of the ensemble members (and as a result, in the composite) in the low-to mid-levels (2–6 km), and stronger perturbation temperatures (at least 8 K) do not develop until 24 h after RI has begun.

Despite these general similarities in inner-core perturbation temperature development, variability in the vertical temperature structure evolution is also present amongst the GOOD composite members. The moderate warming (mostly less than 5 K) that is consistently present in the GOOD members prior to RI is primarily confined to heights below 6 km but can occur as high as 8 km (Fig. 11g). In addition, the magnitude of this pre-RI warming can be as weak as 3 K (Fig. 11c), or as strong as 6.5 K (Fig. 11i). In the 24 h after RI onset, nearly all of the GOOD members have perturbation temperature structures that steadily increase in magnitude up to 6–8 K while extending upwards with height through 10 km. Over the next 24–48 h, the maxima in perturbation temperature develop as the members approach their peak intensities and subsequently begin to decay (Figs. 1b and 1c). However, differences are present in the evolution of the heights at which the maxima exist. In some of the members, perturbation temperatures of at least 9 K first appear ~24 h after RI onset at heights between 4–6 km and steadily increase upwards to ~8 km within ~60 hours after RI onset (Figs. 11b, 11d, and 11f). Other members see the maxima more abruptly rise to ~8 km about 48 h after RI begins (Figs. 11e and 11g). Finally, the stronger perturbation temperatures in the majority of the rest of members develop at heights of 6–8 km and are maintained at this level throughout this period (Figs. 11a, 11c, and 11i).

Factors contributing to the differences in the inner-core temperature structures are next briefly explored. Comprehensive potential temperature budget analyses performed in Stern and Zhang (2013a and b) showed that perturbation temperature maxima are typically confined to the mid-levels due to a secondary maximum in static stability. Meanwhile, the upper-level descent maximum is coincident with a minimum in static stability, which prevents concentrated warming at these heights. In addition, in TCs embedded in moderate vertical wind shear environments (such as Edouard), increased mixing at the eye-eyewall interface is likely. However, strong inertial stability of the vortex can allow for parcels to remain in the eye for several days, influencing the inner-core temperature structure. Following the Stern and Zhang studies, the evolutions of vertical velocity, static, and inertial stability are examined for a few GOOD members (not shown). All of these members maximize descent in the upper-levels and have static stability profiles with secondary maxima in the mid-levels and minima in the upper-levels, which produce a mid-level warm core. However, variability is present in these evolutions as well, as larger magnitudes of mid-level static stability tend to be associated with more significant mid-level perturbation temperature maxima, while stronger and deeper vortices (as indicated by inertial stability) are typically associated with stronger warm cores. These relationships explain some of the variability present in the GOOD inner-core temperature structures, though it should be noted that these variables are only weakly correlated (not shown).

Significant variation in the inner-core perturbation temperature evolution within GOOD (with the strongest warming occurring well after RI onset) despite very similar intensity evolutions suggests that changes in the height and strength of the maximum perturbation temperature are not necessarily associated with TC intensity or subsequent intensity trends. This hypothesis will be explored quantitatively in the next section.

3.7 Analysis of the simulated warm core: Correlation analyses

This section uses correlation analyses to quantitatively examine the potential relationships between the perturbation temperature structure and the TC intensity. Figure 12a shows the correlation between both the height and the strength of the maxima in perturbation temperature and the RI-onset times for the 30 members of the developing composite groups. Both correlations are insignificant over the first 24 h, as no substantial warm core development or changes in TC intensity occur during this time. Over the next 24 h, a weak to moderate correlation between both the height (~0.3) and the strength (~–0.3 to –0.5) of the perturbation temperature maxima and RI-onset time begins to develop, as the GOOD_EARLY members approach RI and warming begins to occur in the low-to mid-levels of only these members.

Between 48 and 96 h, relatively strong correlations have developed (~–0.6 to –0.7) between both the height and strength of the maxima in perturbation temperature and RI onset, suggesting that stronger and higher perturbation temperature maxima occur in the members whose RI onsets occur earlier in the simulation. However, much of this signal is simply a result of the divergent RI onsets rather than a driving factor in RI. Part correlations controlling for minimum SLP can account for this divergence, as the first-order part correlation between two variables while controlling for a third variable effectively treats the third as a constant (e.g., Sippel et al. 2011). Both part correlations controlling for minimum SLP fail to exceed ±0.3, indicating that essentially no relationship exists between the strength or height of the maximum perturbation temperature and the subsequent RI-onset time (Fig. 12a).

To examine whether a broader relationship exists between the overall perturbation temperature structure and RI-onset time in this ensemble, the correlation between the vertically averaged inner-core (within 25-km of the surface center) perturbation temperature and RI-onset for the 30 members of the developing composite groups is also calculated (Fig. 12b). As in the correlations between both the height and the strength of the perturbation temperature maxima, little to no relationship is present over the first 24 h. However, over the next 24 h, a moderate to strong (~–0.5 to –0.8) correlation develops as members begin to approach RI-onset, which remains strong throughout most of the simulation. However, part correlations controlling for minimum SLP drop to zero by 48 h (Fig. 12b), indicating that essentially all of the relationship between vertically averaged inner-core perturbation temperature and RI-onset results from the divergent ensemble intensities. In addition, by 24 h the correlation between the vertically averaged inner-core perturbation temperature and the strength of the perturbation temperature maxima is ~0.9 (Fig. 12b), demonstrating that the behavior of the perturbation temperature maxima is strongly correlated with the broader vertical structure of the inner-core temperature.

Figure 12c shows the evolution of the correlation between the area-averaged (within 25-km radius) vertical profiles of perturbation temperature magnitude and RI-onset time for the members of the developing composites. Between 24 and 48 h, a region of weak to moderate negative correlation (as much as ~–0.6) develops between 2 and 8 km, which is representative of the moderate warming present in the low-to mid-levels of the composites in the times leading up to RI (Figs. 9 and 11). Over the next few days of the simulation, as the various composite groups approach their respective RI-onset times, the correlation grows very significantly throughout much of the vertical profile. This result indicates that the perturbation temperatures increase in magnitude according to earlier RI-onset times. However, when the part correlation controlling for current minimum SLP is calculated (Fig. 12d), the entirety of the significant region of correlation discussed above vanishes, reinforcing the conclusion that the relationship between the inner-core perturbation temperature structure and RI onset results from the diverging intensities in the ensemble. It is therefore unlikely that the evolution of the inner-core temperature structure could be used as a predictor of RI onset in this ensemble. Cross-correlations between RI onset time and warm core development confirm this hypothesis, as the majority of the significantly intensifying members have correlations that peak at lags of 0–6 h after RI onset (not shown).

4. Summary and Conclusions

This study examines the evolution of the inner-core temperature structure of Hurricane Edouard (2014), primarily through high-altitude dropsondes deployed during the 2014 campaign of HS3 and a 60-member WRF-EnKF simulation. This ensemble was originally a 5-day real-time forecast generated by the PSU Atlantic hurricane forecast and analysis system (extended to 7 days in this study), and the resulting ensemble wind field structures have been verified against Doppler wind analyses obtained by the NOAA P-3 aircraft and HS3 dropsondes. Composite groups based on differences in RI-onset timing (first defined in Munsell et al. 2017) are utilized to examine the variability associated with Edouard's warm core development.

Throughout the 16–17 September HS3 flight, two distinct perturbation temperature structures were measured. The profiles of the innermost dropsondes primarily yielded multiple perturbation temperature maxima of ~10–12 K, centered at 4–6 km and at 7–9 km; some dropsondes have an additional maximum ~10 km. Meanwhile, the dropsondes farther away from the surface center observed a single perturbation temperature maxima of ~6–8 K at heights of ~7–9 km. The inner-core perturbation temperature composites of the members of GOOD_LATE, whose intensities agree with Best Track during the 16–17 September flight, also compare favorably with the HS3 observations. The height of the maximum perturbation temperature at Edouard's peak intensity is slightly lower in GOOD_LATE (~6 km) than observed, and no evidence of multiple perturbation temperature maxima is present in the innermost region of Edouard's eye. However, the overall inner-core temperature structure and the magnitude of the perturbation temperature maxima are comparable between the model composite and the observations.

Given this agreement, the increased temporal frequency of the ensemble output allows for additional insight into the development of Edouard's warm core throughout the intensification period to be obtained. Despite as much as 48–60 h of simulation time between RI onset in the GOOD_EARLY, GOOD, and GOOD_LATE members, the evolutions of Edouard's inner-core perturbation temperature have many similarities when compared in an RI-onset time-relative framework. All developing composites indicate some moderate warming (~4 K) in the low-to mid-levels (~2–6 km) ~24–48 h prior to RI, but the most significant warming (> 7 K) is present higher in the inner-core (~8 km) and does not occur until at least 24 h after RI begins.

Despite broad similarities in the evolution of the inner-core temperature structure of the developing composites with respect to RI-onset time, variability is present within the composite groups. The strength of the maximum inner-core perturbation temperature in the GOOD members at peak intensity varies by as much as 3 K (magnitudes of ~9–12 K), and the height at which this maximum occurs can be as low as 5 km or as high as 9 km. In addition, although moderate low- to mid-level warming is present in nearly all of the members ~24 h prior to RI (as in the composite), the magnitude of this warming varies by ~3 K. Approximately 24 h after RI has begun, as stronger inner-core warming begins to occur, the evolution of the height at which the maximum perturbation temperature occurs differs across the members of GOOD. In particular, the warm core steadily builds upwards in height in some members, while other members have perturbation temperature maxima at relatively constant heights. It should be noted that unlike in the Hurricane Wilma (2005) simulation examined in Chen et al. (2011) and Chen and Zhang (2013), no evidence of an upper-tropospheric warm core is present in any of the members prior to RI, and warming at any level never serves as a trigger for RI since the most significant warming always occurs after RI onset.

Although mid-level perturbation temperature maxima always develop in the GOOD members ~24 h after RI onset (primarily due to secondary maxima in static stability at these levels as thoroughly demonstrated in Stern and Zhang 2013b), the causes of the variability in the warm core vertical structure within the composite group (whose members have very similar intensities) need to be explored further. There is some evidence that variations in the strength of the inner-core updrafts, the magnitude of mid-level static stability, and the strength and depth of the intensifying vortex (as measured by inertial stability) can impact the height and strength at which the maximum warming occurs, although these variables are only weakly correlated.

To further examine the relationships between inner-core temperature structure and TC intensity more quantitatively, additional correlation analyses are performed. At times throughout the simulation window, the correlation between both the strength and height of the perturbation temperature maxima and RI onset approach moderate to strong values. This is mostly a result of ensemble divergence and not a causal factor for RI in the ensemble, as illustrated by insignificant part correlations controlling for current minimum SLP. These results imply that there is little to no relationship between the strength or height of the maximum perturbation temperature and subsequent TC intensity changes, consistent with Stern and Zhang (2016) and Komaromi and Doyle (2016). In addition, the correlation between RI onset and the moderate warming in the low-to mid-levels that is observed ~24 h prior to RI also becomes insignificant when controlling for current intensity. This similarly suggests that thermodynamic changes in the inner-core of Edouard likely occur either in tandem with or after intensification has already commenced and are therefore not a useful predictor of RI onset in this ensemble.

The conclusion in this study that inner-core temperature structure is unrelated to future intensity changes in the Edouard ensemble is similar to conclusions reached by Stern and Zhang (2016) and Komaromi and Doyle (2016), which used dropsondes and a deterministic simulation from a single TC (Hurricane Earl 2010) and high-altitude dropsondes from a variety of TCs sampled during HS3 to demonstrate this same point. In addition, despite very similar intensity evolutions within the GOOD composite group, considerable variability exists in the exact temperature structure of the inner-core as significant differences are present in the precise height and strength of the perturbation temperature maxima. Therefore, the intensity of the TC does not dictate the exact details of the vertical profile of inner-core temperature structure.

Acknowledgements: This work is supported by the NASA New Investigator Program (Grant NNX12AJ79G, NNX15AF38G, and NNX16AI21G), the Office of Naval Research (Grant N000140910526), the National Science Foundation (Grant AGS-1305798), NASA's Hurricane Science Research Program (HSRP), the Hurricane and Severe Storm Sentinel (HS3) investigation under NASA's Earth Venture Program, and NOAA's Hurricane Forecast Improvement Program (HFIP). The research was performed in part while the first author was appointed as a NASA Postdoctoral Program fellow at the Goddard Space Flight Center (GSFC), administered by USRA through a contract with NASA. Computing was performed at the Texas Advanced Computing Center (TACC). We thank Yonghui Weng for conducting the PSU WRF-EnKF analysis and forecasting of the event, Derrick Herndon for providing the University of Wisconsin/CIMSS processed AMSU-A satellite data, and Daniel Stern and two anonymous reviewers for beneficial comments on an earlier version of the manuscript. We also thank NOAA/HRD for making the P-3 Doppler radar analyses available and Daniel Stern for providing code to help visualize this data.

5. References

Barker, D. M., W. Huang, Y.-R. Guo, A. J. Bourgeois, and Q. N. Xiao, 2004: A three-dimensional variational data assimilation system for MM5: Implementation and initial results. *Mon. Wea. Rev.*, **132**, 897–914.

Braun, S. A., and Coauthors, 2013: NASA's Genesis and Rapid Intensification Processes (GRIP) field experiment. *Bull. Amer. Meteor. Soc.*, **94**, 345–363, doi: 10.1175/BAMS-D-11-00232.1.

Braun, S. A., P. A. Newman, and G. M. Heymsfield, 2016: NASA's Hurricane and Severe Storm Sentinel (HS3) investigation. *Bull. Amer. Meteor. Soc.*, **97**, 2085–2102, doi: 10.1175/BAMS-D-15-00186.1.

Chen, H., and S. G. Gopalakrishnan, 2015: A study on the asymmetric rapid intensification of Hurricane Earl (2010) using the HWRF system. *J. Atmos. Sci.*, **72**, 531–550, doi: 10.1175/JAS-D-14-0097.1.

Chen, H., and D.-L. Zhang, 2013: On the rapid intensification of Hurricane Wilma (2005). Part II: Convective bursts and the upper-level warm core. *J. Atmos. Sci.*, **70**, 146–162, doi: 10.1175/JAS-D-12-062.1.

Chen, H., D.-L. Zhang, J. Carton, and R. Atlas, 2011: On the rapid intensification of Hurricane Wilma (2005). Part I: Model prediction and structural changes. *Wea. Forecasting*, **26**, 885–901, doi: 10.1175/WAF-D-11-00001.1.

Dunion, J. P., 2011: Rewriting the climatology of the tropical North Atlantic and Caribbean Sea atmosphere. *J. Climate*, **24**, 893–908, doi: 10.1175/2010JCLI3496.1.

Durden, S. L., 2013: Observed tropical cyclone eye thermal anomaly profiles extending above 300 hPa. *Mon. Wea. Rev.*, **141**, 4256–4268, doi: 10.1175/MWR-D-13-00021.1.

Fang, J., O. Pauluis, and F. Zhang, 2017: Isentropic analysis on the intensification of Hurricane Edouard (2014). *J. Atmos. Sci*, in review.

Gamache, J. F., J. S. Griffin Jr., P. P. Dodge, and N. F. Griffin, 2004: Automatic Doppler analysis of three-dimensional wind fields in hurricane eyewalls. *26th Conf. on Hurricanes and Tropical Meteorology*, Miami, FL, Amer. Meteor. Soc., 5D.4. [Available online at http://ams.confex.com/ams/pdfpapers/75806.pdf.]

Halverson, J. B., J. Simpson, G. Heymsfield, H. Pierce, T. Hock, and L. Ritchie, 2006: Warm core structure of Hurricane Erin diagnosed from high altitude dropsondes during CAMEX-4. *J. Atmos. Sci.*, **63**, 309–324.

Hawkins, H. F., and S. M. Imbembo, 1976: The structure of a small, intense hurricane–Inez 1966. *Mon. Wea. Rev.*, **104**, 418–442.

Hawkins, H. F., and D. T. Rubsam, 1968: Hurricane Hilda, 1964. II: Structure and budgets of the hurricane on October 1, 1964. *Mon. Wea. Rev.*, **96**, 617–636.

Jordan, C. L., 1958: Mean soundings for the West Indies area. *J. Meteor.*, **15**, 91–97.

Knaff, J. A., S. A. Seseske, M. DeMaria, and J. L. Demuth, 2004: On the influences of vertical wind shear on symmetric tropical cyclone structure derived from AMSU. *Mon. Wea. Rev.*, **132**, 2503–2510.

Komaromi, W. A., and J. D. Doyle, 2016: Tropical cyclone outflow and warm core structure as revealed by HS3 dropsonde data. *Mon. Wea. Rev.*, doi: 10.1175/MWR-D-16-0172.1, in press.

La Seur, N. E., and H. F. Hawkins, 1963: An analysis of Hurricane Cleo (1958) based on data from research reconnaissance aircraft. *Mon. Wea. Rev.*, **91**, 694–709.

Melhauser, C., F. Zhang, Y. Weng, Y. Jin, H. Jin and Q. Zhao, 2017: A multiple-model convection-permitting ensemble examination of the probabilistic prediction of tropical cyclones: Hurricanes Sandy (2012) and Edouard (2014). *Wea. Forecasting*, **32**, 665-688, doi: 10.1175/WAF-D-16-0082.1.

Munsell, E. B., J. A. Sippel, S. A. Braun, Y. Weng, and F. Zhang, 2015: Dynamics and predictability of Hurricane Nadine (2012) evaluated through convection-permitting ensemble analysis and forecasts. *Mon. Wea. Rev.*, **143**, 4513–4532, doi: 10.1175/MWR-D-14-00358.1.

Munsell, E. B., and F. Zhang, 2014: Prediction and uncertainty of Hurricane Sandy (2012) explored through a real-time cloud-permitting ensemble analysis and forecast system assimilating airborne Doppler radar observations. *J. Adv. Model. Earth Syst.*, **6**, 38–58, doi: 10.1002/2013MS000297.

Munsell, E. B., F. Zhang, J. A. Sippel, S. A. Braun, and Y. Weng, 2017: Dynamics and predictability of the intensification of Hurricane Edouard (2014). *J. Atmos. Sci.*, in press, doi: 10.1175/JAS-D-16-0018.1.

Munsell, E. B., F. Zhang, and D. P. Stern, 2013: Predictability and dynamics of a non-intensifying tropical storm: Erika (2009). *J. Atmos. Sci.*, **70**, 2505–2524.

Ohno, T., and M. Satoh, 2015: On the warm core of a tropical cyclone formed near the tropopause. *J. Atmos. Sci.*, **72**, 551–571, doi: 10.1175/JAS-D-14-0078.1.

Revercomb, H. E., 2015: Hurricane and Severe Storm Sentinel (HS3) Scanning High-Resolution Interferometer Sounder (S-HIS). Dataset available online [https://hs3.nsstc.nasa.gov/pub/hs3/SHIS/] from the NASA Global Hydrology Resource Center DAAC, Huntsville, Alabama, U.S.A., doi: http://dx.doi.org/10.5067/HS3/SHIS/DATA201.

Rios-Berrios, R., R. D. Torn, and C. A. Davis, 2015: An ensemble approach to investigate tropical cyclone intensification in sheared environments. Part I: Katia (2011). *J. Atmos. Sci.*, **73**, 71–93, doi: 10.1175/JAS-D-15-0052.1.

Rogers, R. F., and Coauthors, 2013a: NOAA's Hurricane Intensity Forecasting Experiment: A progress report. *Bull. Amer. Meteor. Soc.*, **94**, 859–882, doi: 10.1175/BAMS-D-12-00089.1.

Rogers, R. F., J. A. Zhang, J. Zawislak, H. Jiang, G. R. Alvey, E. J. Zipser, and S. N. Stevenson, 2016: Observations of the structure and evolution of Hurricane Edouard (2014) during intensity change. Part II: Kinematic structure and the distribution of deep convection. *Mon. Wea. Rev.*, **144**, 3355–3376, doi: 10.1175/MWR-D-16-0017.1.

Skamarock, W. C., and Coauthors, 2008: A description of the Advanced Research WRF version 3. NCAR/TN–4751STR, 113 pp. [Available online at http://www2.mmm.ucar.edu/wrf/users/docs/arw_v3.pdf.]

Sippel, J. A., S. A. Braun, and C.-L. Shie, 2011: Environmental influences on the strength of Tropical Storm Debby (2006). *J. Atmos. Sci.*, **68**, 2557–2581.

Stern, D. P., and D. S. Nolan, 2009: Reexamining the vertical structure of tangential winds in tropical cyclones: Observations and theory. *J. Atmos. Sci.*, **66**, 3579–3600, doi: 10.1175/2009JAS2916.1.

Stern, D. P., and D. S. Nolan, 2012: On the height of the warm core in tropical cyclones. *J. Atmos. Sci.,* **69**, 1657–1680, doi: 10.1175/JAS-D-11-010.1.

Stern, D. P., and F. Zhang, 2013a: How does the eye warm? Part I: A potential temperature budget analysis of an idealized tropical cyclone. *J. Atmos. Sci.*, **70**, 73–90, doi: 10.1175/JAS-D-11-0329.1.

Stern, D. P., and F. Zhang, 2013b: How does the eye warm? Part II: Sensitivity to vertical wind shear and a trajectory analysis. *J. Atmos. Sci.*, **70**, 1849–1873, doi: 10.1175/JAS-D-12-0258.1.

Stern, D. P., and F. Zhang, 2016: The warm-core structure of Hurricane Earl (2010). *J. Atmos. Sci.*, **73**, 3305–3328, doi: 10.1175/JAS-D-15-0328.1.

Stewart, S. R., 2014: Tropical cyclone report: Hurricane Edouard (AL062014). NOAA/National Hurricane Center Tech. Rep. AL062014, 19 pp. [Available online at http://www.nhc.noaa.gov/data/tcr/AL062014_Edouard.pdf.]

Tang, X., Z. Tan, J. Fang, Y.Q. Sun, and F. Zhang, 2017: Impacts of the diurnal radiation cycle on secondary eyewall formation. *J. Atmos. Sci.*, doi: 10.1175/JAS-D-17-0020.1, in press.

Tang, X., and F. Zhang, 2016: Impacts of the diurnal radiation cycle on the formation, intensity and structure of Hurricane Edouard (2014). *J. Atmos. Sci.*, **73**, 2871-2892, doi: 10.1175/JAS-D-15-0283.1.

Wang, H., and Y. Wang, 2014: A numerical study of Typhoon Megi (2010). Part I: Rapid intensification. *Mon. Wea. Rev.*, **142**, 29–48, doi: 10.1175/MWR-D-13-00070.1.

Weng, Y., and F. Zhang, 2012: Assimilating airborne Doppler radar observations with an ensemble Kalman filter for convection-permitting hurricane initialization and prediction: Katrina (2005). *Mon. Wea. Rev.*, **140**, 841–859, doi: 10.1175/2011MWR3602.1.

Weng, Y., and F. Zhang, 2016: Advances in convection-permitting tropical cyclone analysis and prediction through EnKF assimilation of reconnaissance aircraft observations. *J. Meteor. Soc. Japan*, **94**, 345–358.

Wick, G., 2015: Hurricane and Severe Storm Sentinel (HS3) Global Hawk AVAPS Dropsonde System [2014 RF05–08]. Dataset available online [https://hs3.nsstc.nasa.gov/pub/hs3/AVAPS/] from the NASA Global Hydrology Resource Center DAAC, Huntsville, Alabama, U.S.A. doi:10.5067/HS3/AVAPS/DROPSONDE/DATA201.

Willoughby, H. E., 1990: Gradient balance in tropical cyclones. *J. Atmos. Sci.*, **47**, 265–274.

Young, K., T. Hock, and C. Martin, 2014: Hurricane and Severe Storm Sentinel (HS3) 2014 dropsonde data quality report. National Center for Atmospheric Research (NCAR) Earth Observing Lab (EOL), Boulder, Colorado, U.S.A. [Available online at http://data.eol.ucar.edu/datafile/nph-get/348.004/readme.HS3-2014.GHdropsonde.pdf].

Zawislak, J., H. Jiang, G. R. Alvey, E. J. Zipser, R. F. Rogers, J. A. Zhang, and S. N. Stevenson, 2016: Observations of the structure and evolution of Hurricane Edouard (2014) during intensity change. Part I: Relationship between the thermodynamic structure and precipitation. *Mon. Wea. Rev.*, **144**, 3333–3354. doi: 10.1175/MWR-D-16-0018.1.

Zhang, F., and Y. Weng, 2015: Predicting hurricane intensity and associated hazards: A five-year real-time forecast experiment with assimilation of airborne Doppler radar observations. *Bull. Amer. Meteor. Soc.*, **96**, 25–32.

Zhang, F., Y. Weng, J. F. Gamache, and F. D. Marks, 2011: Performance of convection-permitting hurricane initialization and prediction during 2008–2010 with ensemble data assimilation of inner-core airborne Doppler radar observations. *Geophys. Res. Lett.*, **38**, L15810.

Zhang F., Y. Weng, J. A. Sippel, Z. Meng, and C. H. Bishop, 2009: Cloud-resolving hurricane initialization and prediction through assimilation of Doppler radar observations with an ensemble Kalman filter: Humberto (2007). *Mon. Wea. Rev.*, **137**, 2105–2125.

Figure Captions

Figure 1. A comparison of the NHC Best Track with deterministic and ensemble forecasts of (a) track, (b) minimum sea level pressure (SLP; hPa) and (c) maximum 10-m wind speed (kt) for the 1200 UTC 11 September 2014 initialization of Hurricane Edouard from the PSU WRF-EnKF system. Members are placed in composite groups of 10 according to their RI-onset time (GOOD; blue, GOOD_EARLY; green, GOOD_LATE; magenta, and POOR; red) and have been extended to 7-day forecasts (the operational real-time system only produces 126-h forecasts). The composite means (thick; positions marked every 12 h in (a)), the NHC Best Track (black; positions marked every 12 h in (a)), and the 5-day APSU deterministic forecast (orange) are also plotted. The remaining ensemble members not classified in composite groups (Other; cyan) remain as 5-day forecasts. Sea surface temperatures (constant throughout simulation) are contoured (filled every 1 K starting at 288 K) in (a). The times that the NOAA P-3 (gray markers) and the 16–17 September flight of NASA's Global Hawk (dark gray markers) sampled Edouard are shown in the top of (b) and (c).

Figure 2. Storm-centered horizontal cross sections of composite 2-km wind speed (ground-relative; contours filled every 2 m s^{-1}) for NOAA P-3 flights in Edouard (top row), GOOD (middle row), and GOOD_LATE (bottom row) at approximately (a,d,g) 1500 UTC 14 September 2014 (75 h), (b,e,h) 1500 UTC 15 September 2014 (99 h), and (c,f,i) 1800 UTC 16 September 2014 (126 h). The 2-km wind speed as measured by the AVAPS dropsondes deployed between 1500 UTC 16 September 2014 and 0900 UTC 17 September 2014 (123–141 h) during the HS3 Global Hawk flight are indicated on (c).

Figure 3. As in Fig. 2, but for azimuthally averaged vertical cross sections of composite tangential winds (contours filled every 2 m s^{-1}).

Figure 4. Vertical profiles from the inner-core (within 50-km of the surface center) AVAPS dropsondes of the (a) distance from Edouard's surface center (km), (b) winds (m s^{-1}), (c) equivalent potential temperature (K), and (d) perturbation temperature (K) with respect to the mean environmental reference profile calculated from the temperatures measured by the dropsondes deployed between 300-km and 700-km from Edouard's surface center during the 16–17 September HS3 Global Hawk flight. All profiles are colored (every 5-km from 0 to 50-km) according to the mean distance from Edouard's surface center that the dropsonde traveled.

Figure 5. As in Fig. 4d, but only for the dropsondes deployed within 20-km of Edouard's surface center. The seven dropsondes fell within (a) 1 km, (b) 4 km, (c), 7 km, (d), 10 km, (e) 14 km, (f), 15 km, and (g) 18 km throughout the 16–17 September HS3 Global Hawk flight.

Figure 6. Radius-height cross section of azimuthal-mean perturbation temperature (K; contours filled every 0.5 K) for the (a) GOOD_LATE composite at 0000 UTC 17 September 2014, (b) the inner-core AVAPS dropsondes deployed during the 16–17 September 2014 HS3 Global Hawk flight, (c) the S-HIS data from the same HS3 flight, and (d) CIMSS-processed AMSU-A data from 2025 UTC 16 September 2014. The azimuthal-mean temperature between 300- to 700-km from the surface center of the GOOD_LATE composite is used as a reference profile in (a)-(c),

while (d) utilizes temperature retrievals averaged at various points ~500 km from the TC surface center.

Figure 7. AVAPS dropsonde (red; binned every 3 h) and GOOD_LATE composite (blue) inner-core (within 50-km from Edouard's surface center) perturbation temperature (K) evolutions for the times in which the dropsondes were deployed (1500 UTC 16 September 2014–0900 UTC 17 September 2014; 123–141 h) for various layer-averaged altitude ranges: (a) 4–6-km, (b) 6–8-km, and (c) 8–10-km. Azimuthal-mean temperature averaged over a 300- to 700-km radius from Edouard's surface center is again used as a reference profile. The shaded regions in (a), (b), and (c) show +/– 1 standard deviation from the mean. (d) Scatterplot of the height of the maximum perturbation temperature (300–700-km environmental temperature reference profile; filled markers every 0.5 K) by radius for the inner-core AVAPS dropsondes (circles) and the GOOD_LATE composite (squares).

Figure 8. As in Fig. 6, but for the (a) GOOD_EARLY, (b) GOOD, (c), GOOD_LATE, and (d) POOR composites at 0000 UTC 17 September 2014.

Figure 9. Evolution of the area-averaged (within 25-km of the surface center) perturbation temperature vertical structure (contours filled every 0.5 K) for the (a) GOOD_EARLY, (b) GOOD, (c) GOOD_LATE, and (d) POOR composites. The dashed black line in (a), (b), and (c) corresponds to the RI-onset time of each respective composite group; RI onset does not occur in the POOR composite.

Figure 10. As in Fig. 6, but for 9 (randomly chosen) of the 10 members of the GOOD composite group at 0000 UTC 17 September 2014.

Figure 11. As in Fig. 9, but for 9 (as in Fig. 10) of the 10 members of the GOOD composite group. Black dashed lines indicate the mean RI-onset time of GOOD.

Figure 12. (a) Evolution of the correlation (solid) and part correlation controlling for minimum SLP (dashed) between the RI times of the 30 developing composite group members and both the height (purple) and the strength of the maximum perturbation temperature (orange). (b) As in (a), but for the vertically averaged inner-core (within 25-km of the surface center) perturbation temperature (magenta). Correlation between the vertically averaged inner-core perturbation temperature and the strength of the maximum perturbation temperature is also plotted (dark blue). (c) Time-height correlation between the strength of the maximum perturbation temperature and the RI-onset time of the 30 members of the developing composite groups. (d) As in (c), but for the part correlation controlling for the current intensity (minimum SLP).

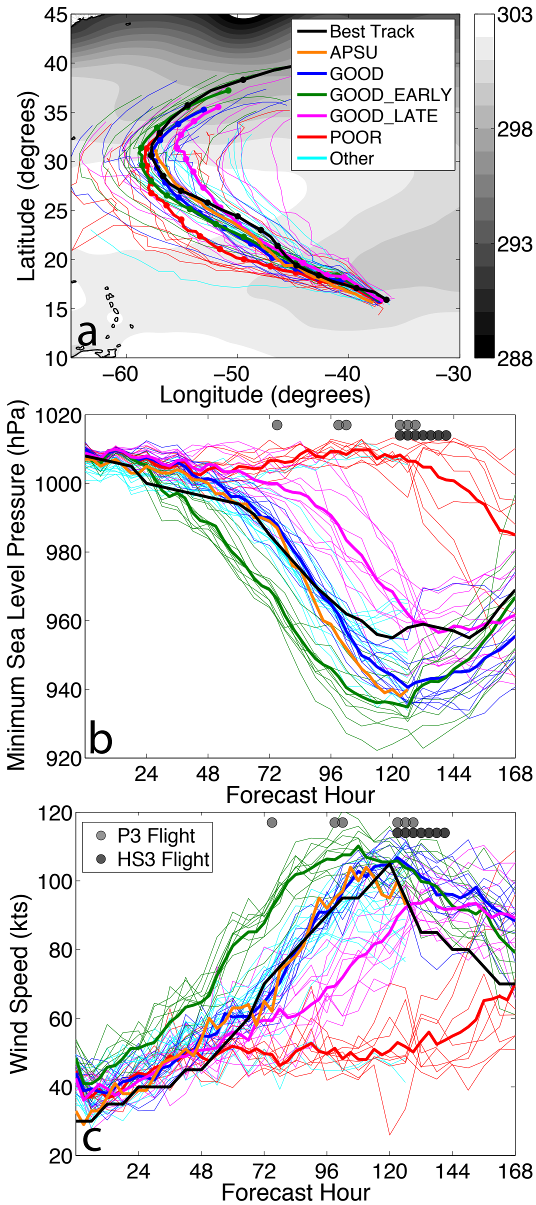

Figure 1. A comparison of the NHC Best Track with deterministic and ensemble forecasts of (a) track, (b) minimum sea level pressure (SLP; hPa) and (c) maximum 10-m wind speed (kt) for the 1200 UTC 11 September 2014 initialization of Hurricane Edouard from the PSU WRF-EnKF system. Members are placed in composite groups of 10 according to their RI-onset time (GOOD; blue, GOOD_EARLY; green, GOOD_LATE; magenta, and POOR; red) and have been extended to 7-day forecasts (the operational real-time system only produces 126-h forecasts). The composite means (thick; positions marked every 12 h in (a)), the NHC Best Track (black; positions marked every 12 h in (a)), and the 5-day APSU deterministic forecast (orange) are also plotted. The remaining ensemble members not classified in composite groups (Other; cyan) remain as 5-day forecasts. Sea surface temperatures (constant throughout simulation) are contoured (filled every 1 K starting at 288 K) in (a). The times that the NOAA P-3 (gray markers) and the 16–17 September flight of NASA's Global Hawk (dark gray markers) sampled Edouard are shown in the top of (b) and (c).

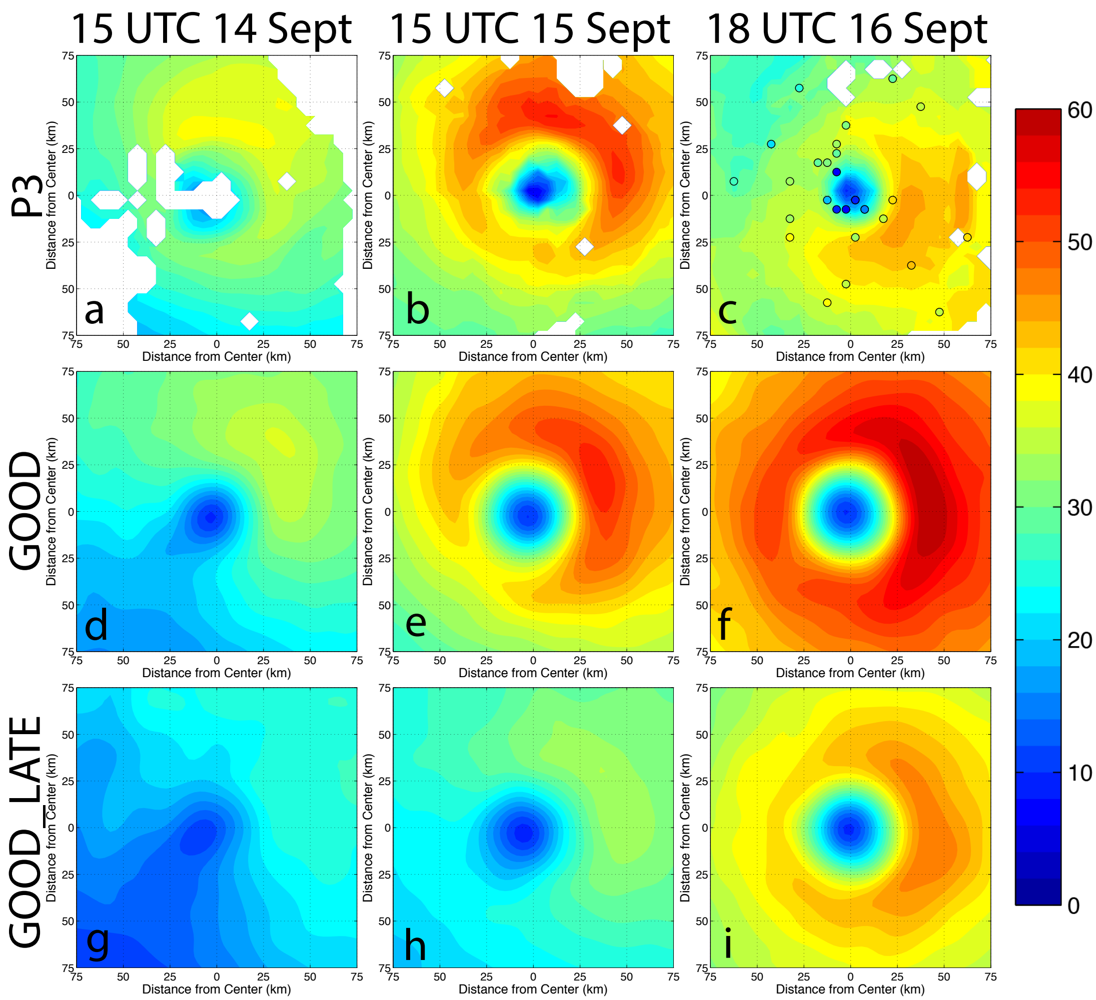

Figure 2. Storm-centered horizontal cross sections of composite 2-km wind speed (ground-relative; contours filled every 2 m s^{-1}) for NOAA P-3 flights in Edouard (top row), GOOD (middle row), and GOOD_LATE (bottom row) at approximately (a,d,g) 1500 UTC 14 September 2014 (75 h), (b,e,h) 1500 UTC 15 September 2014 (99 h), and (c,f,i) 1800 UTC 16 September 2014 (126 h). The 2-km wind speed as measured by the AVAPS dropsondes deployed between 1500 UTC 16 September 2014 and 0900 UTC 17 September 2014 (123–141 h) during the HS3 Global Hawk flight are indicated on (c).

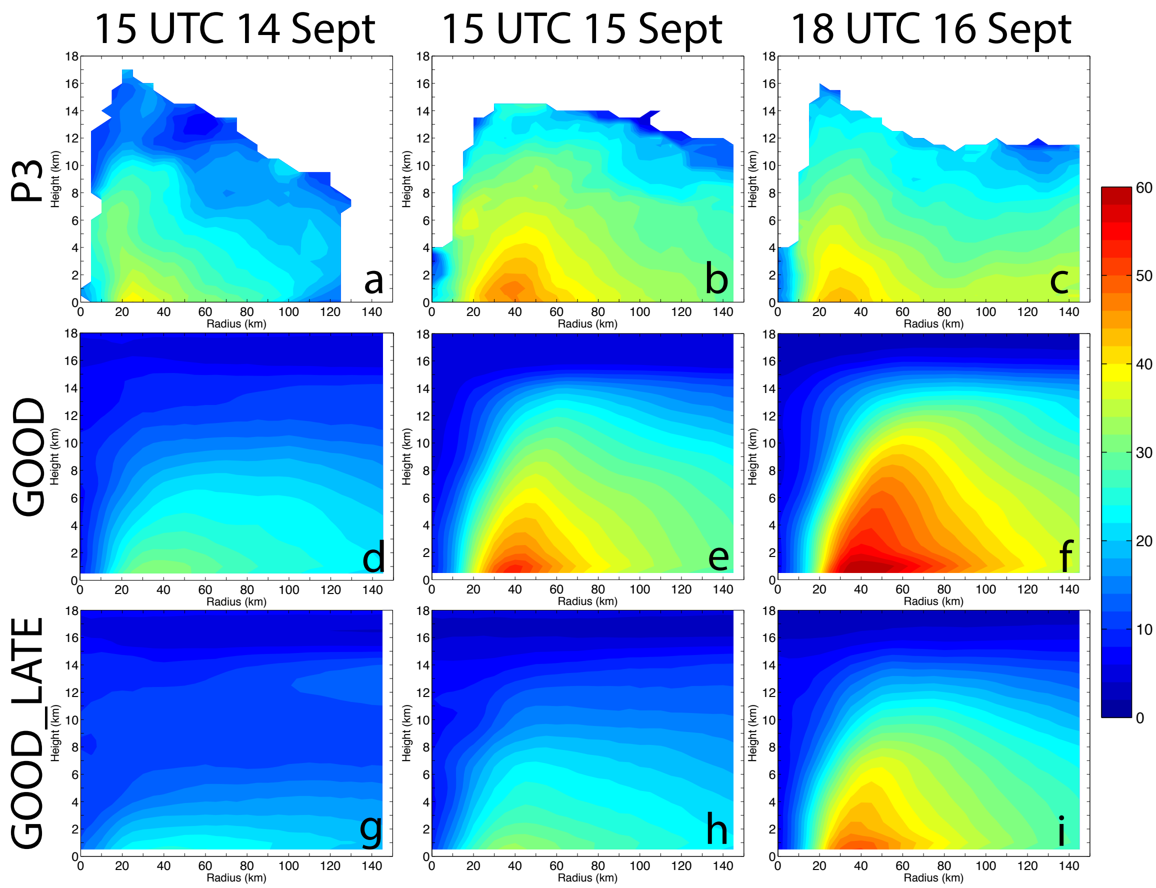

Figure 3. As in Fig. 2, but for azimuthally averaged vertical cross sections of composite tangential winds (contours filled every 2 m s^{-1}).

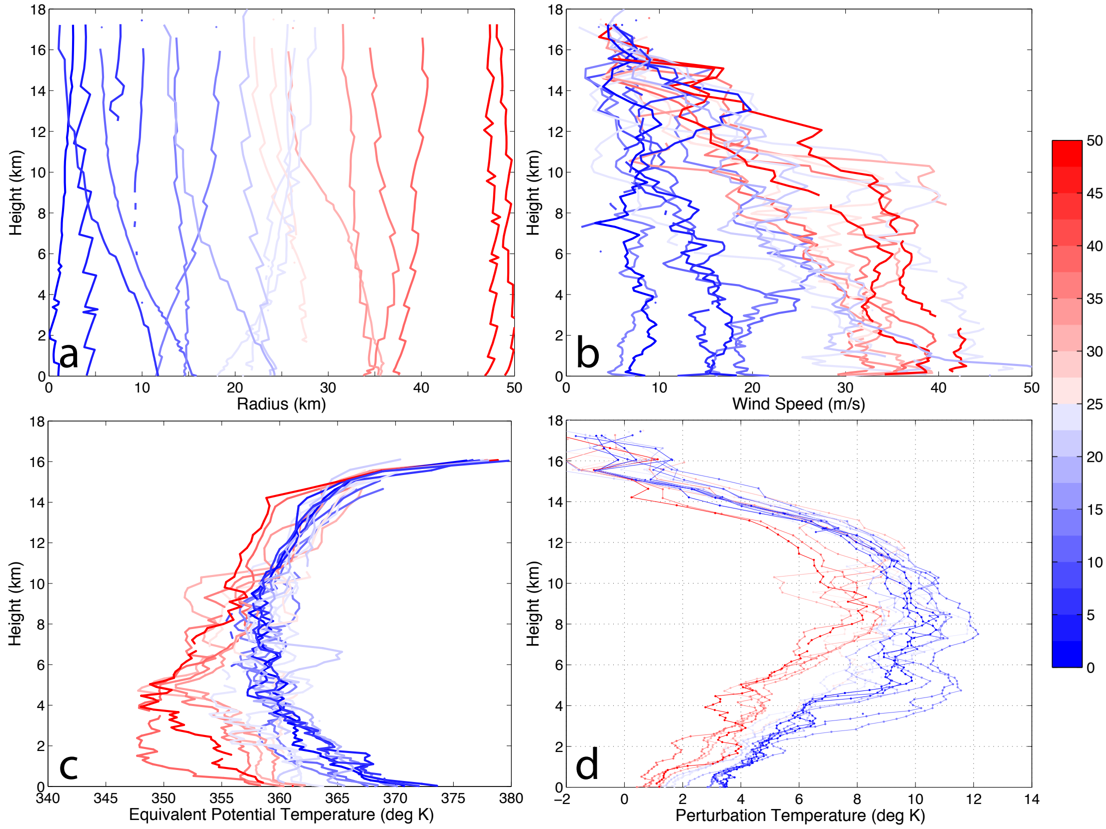

Figure 4. Vertical profiles from the inner-core (within 50-km of the surface center) AVAPS dropsondes of the (a) distance from Edouard's surface center (km), (b) winds (m s^{-1}), (c) equivalent potential temperature (K), and (d) perturbation temperature (K) with respect to the mean environmental reference profile calculated from the temperatures measured by the dropsondes deployed between 300-km and 700-km from Edouard's surface center during the 16–17 September HS3 Global Hawk flight. All profiles are colored (every 5-km from 0 to 50-km) according to the mean distance from Edouard's surface center that the dropsonde traveled.

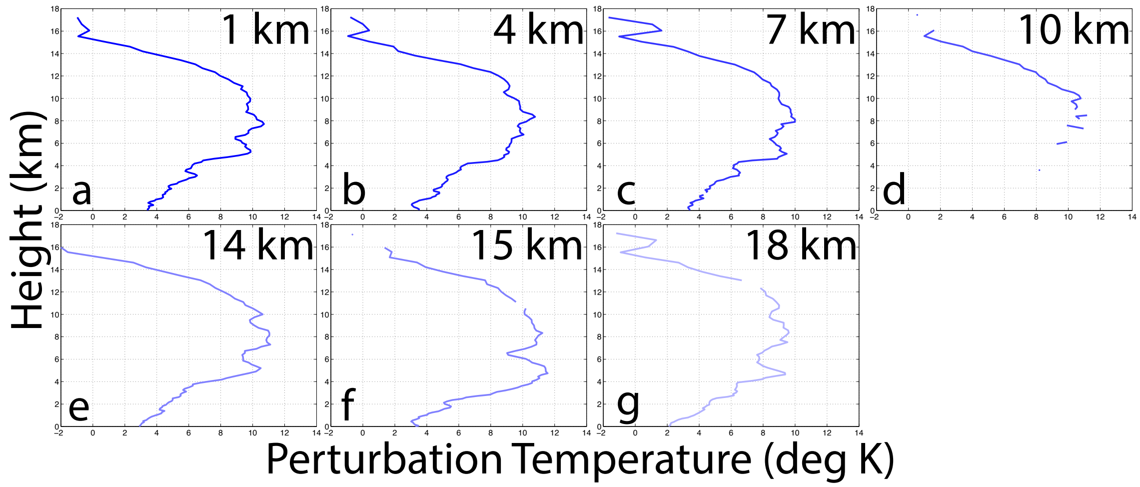

Figure 5. As in Fig. 4d, but only for the dropsondes deployed within 20-km of Edouard's surface center. The seven dropsondes fell within (a) 1 km, (b) 4 km, (c), 7 km, (d), 10 km, (e) 14 km, (f), 15 km, and (g) 18 km throughout the 16–17 September HS3 Global Hawk flight.

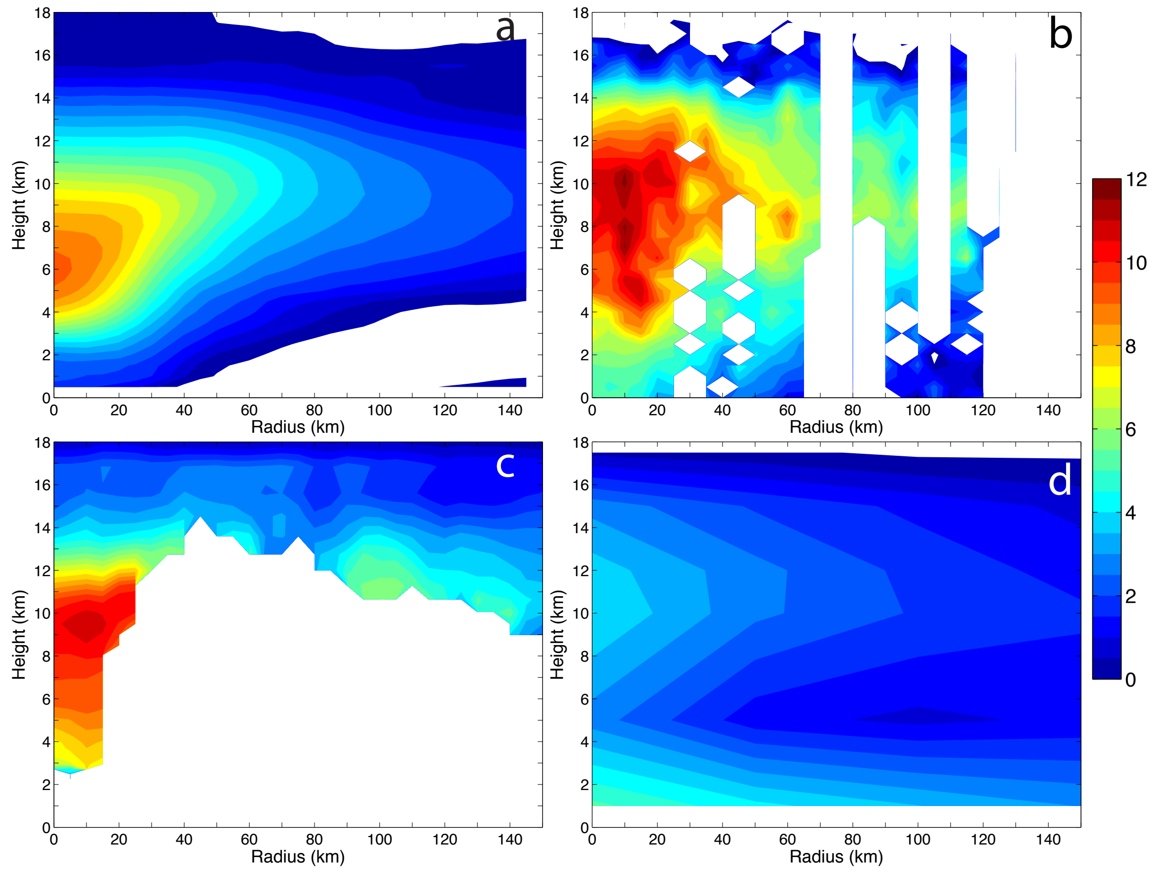

Figure 6. Radius-height cross section of azimuthal-mean perturbation temperature (K; contours filled every 0.5 K) for the (a) GOOD_LATE composite at 0000 UTC 17 September 2014, (b) the inner-core AVAPS dropsondes deployed during the 16–17 September 2014 HS3 Global Hawk flight, (c) the S-HIS data from the same HS3 flight, and (d) CIMSS-processed AMSU-A data from 2025 UTC 16 September 2014. The azimuthal-mean temperature between 300- to 700-km from the surface center of the GOOD_LATE composite is used as a reference profile in (a)-(c), while (d) utilizes temperature retrievals averaged at various points ~500 km from the TC surface center.

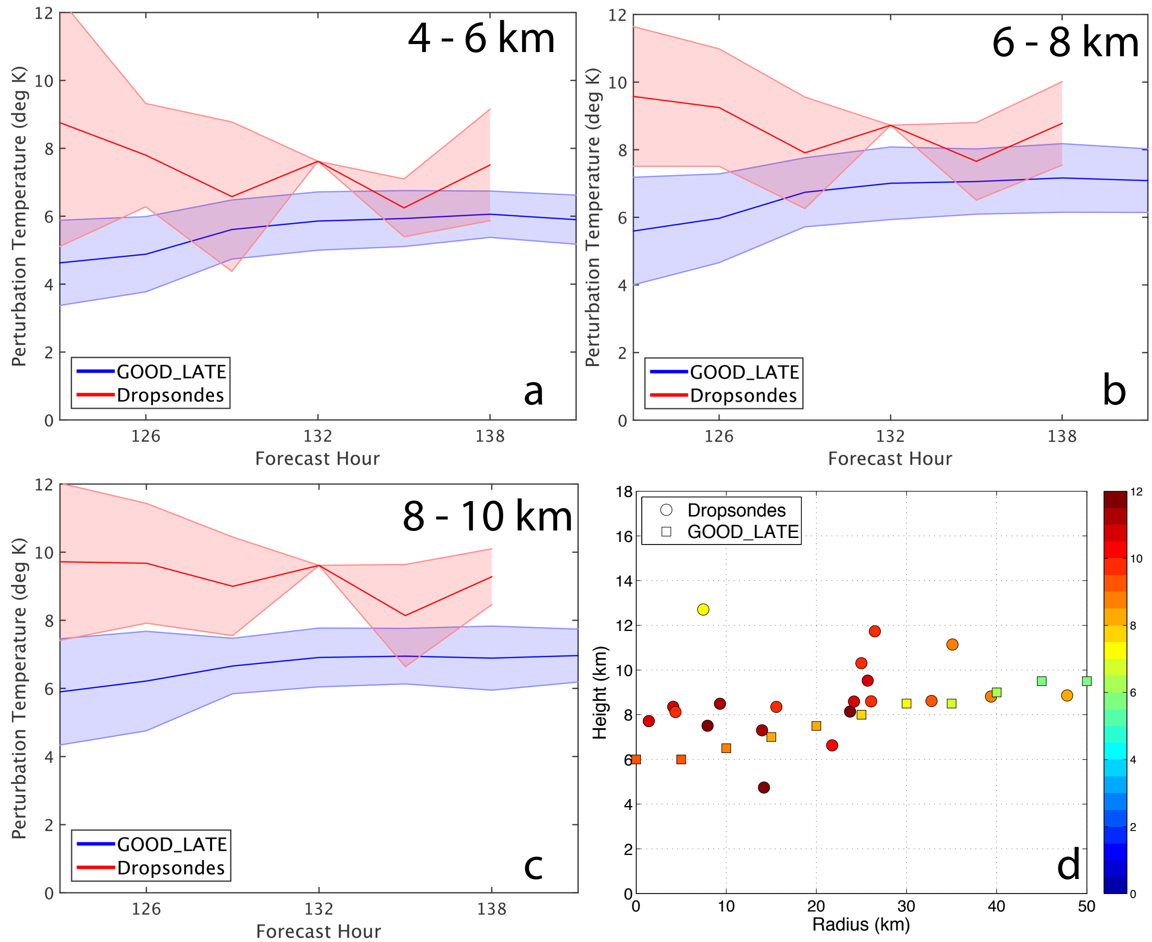

Figure 7. AVAPS dropsonde (red; binned every 3 h) and GOOD_LATE composite (blue) inner-core (within 50-km from Edouard's surface center) perturbation temperature (K) evolutions for the times in which the dropsondes were deployed (1500 UTC 16 September 2014–0900 UTC 17 September 2014; 123–141 h) for various layer-averaged altitude ranges: (a) 4–6-km, (b) 6–8-km, and (c) 8–10-km. Azimuthal-mean temperature averaged over a 300- to 700-km radius from Edouard's surface center is again used as a reference profile. The shaded regions in (a), (b), and (c) show +/– 1 standard deviation from the mean. (d) Scatterplot of the height of the maximum perturbation temperature (300–700-km environmental temperature reference profile; filled markers every 0.5 K) by radius for the inner-core AVAPS dropsondes (circles) and the GOOD_LATE composite (squares).

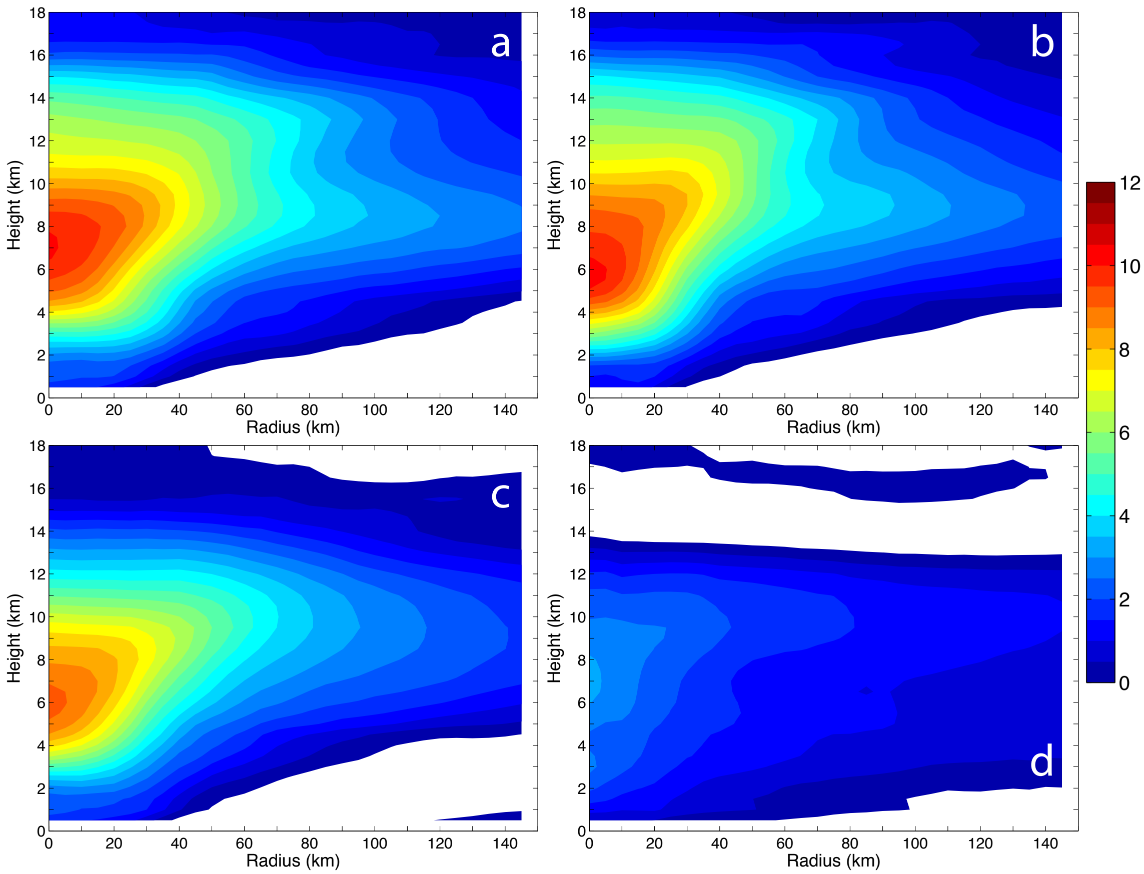

Figure 8. As in Fig. 6, but for the (a) GOOD_EARLY, (b) GOOD, (c), GOOD_LATE, and (d) POOR composites at 0000 UTC 17 September 2014.

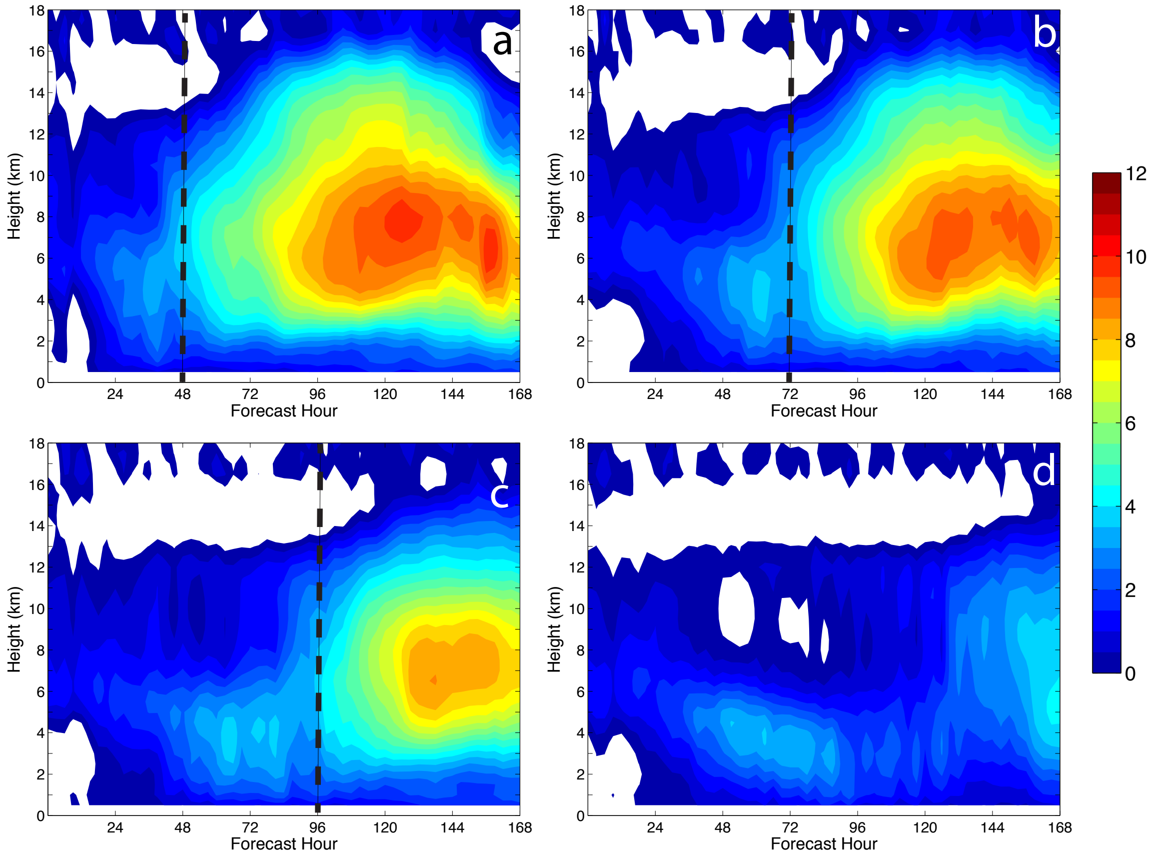

Figure 9. Evolution of the area-averaged (within 25-km of the surface center) perturbation temperature vertical structure (contours filled every 0.5 K) for the (a) GOOD_EARLY, (b) GOOD, (c) GOOD_LATE, and (d) POOR composites. The dashed black line in (a), (b), and (c) corresponds to the RI-onset time of each respective composite group; RI onset does not occur in the POOR composite.

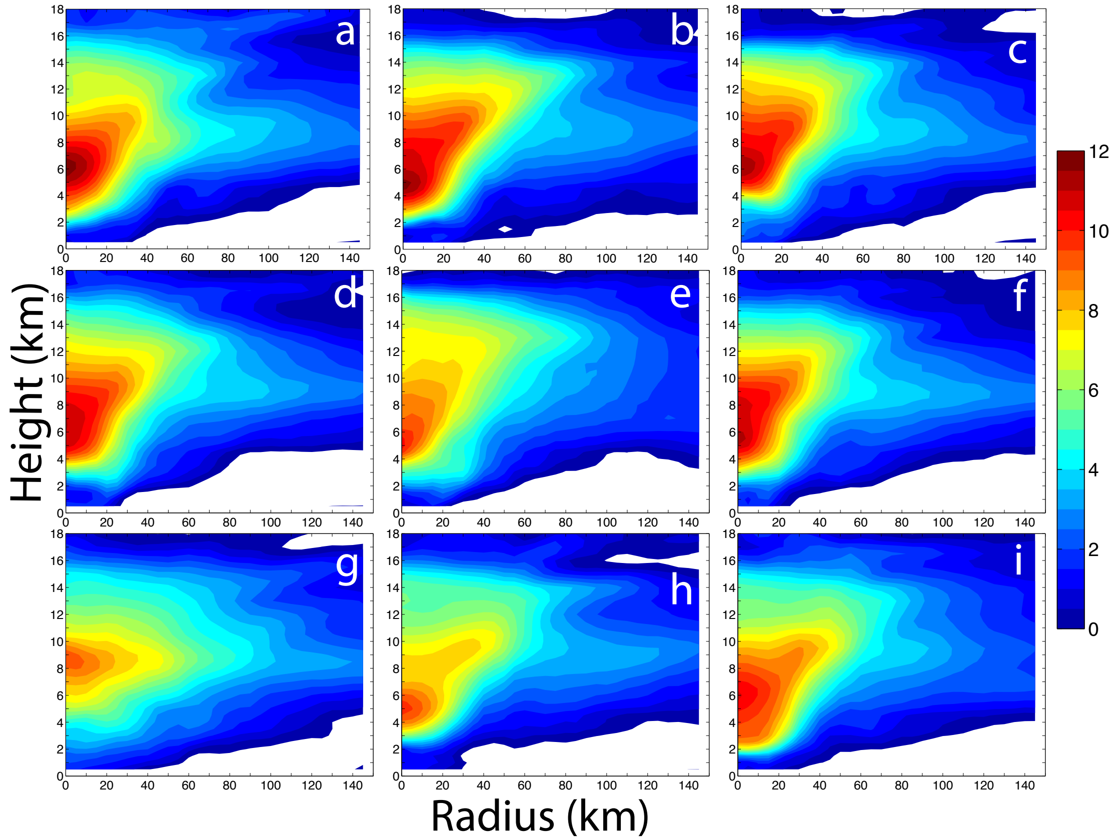

Figure 10. As in Fig. 6, but for 9 (randomly chosen) of the 10 members of the GOOD composite group at 0000 UTC 17 September 2014.

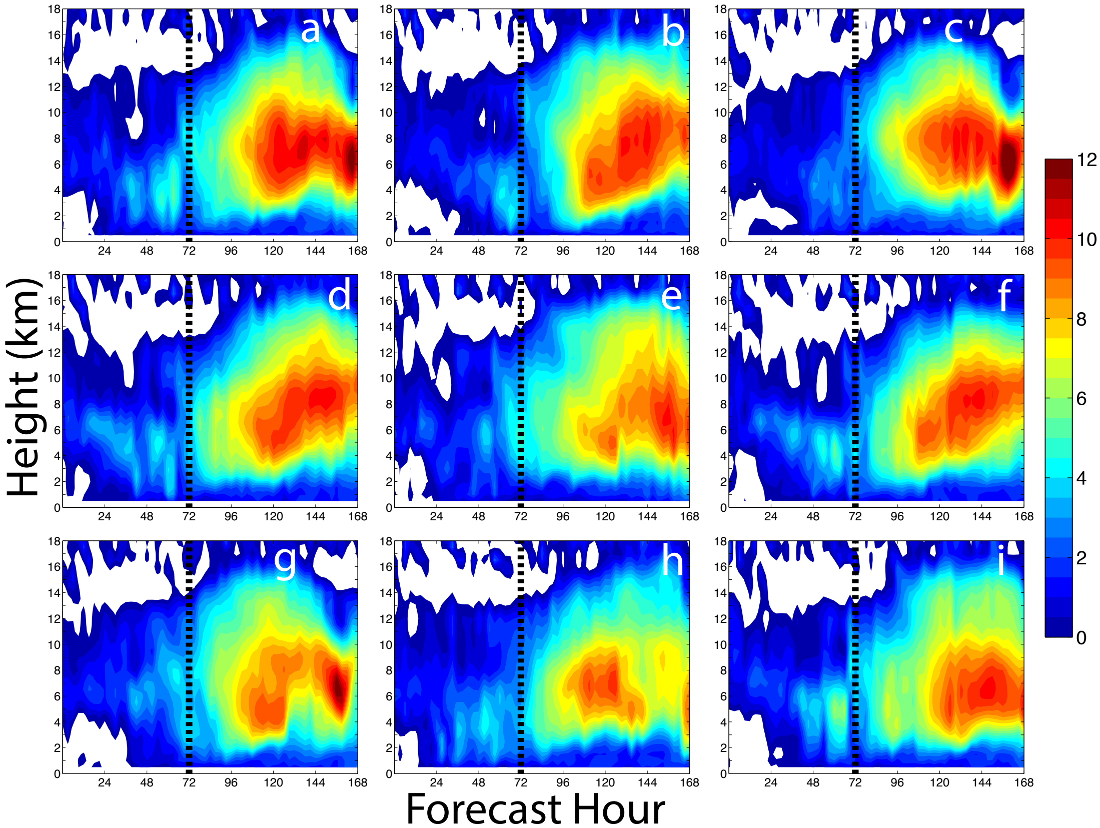

Figure 11. As in Fig. 9, but for 9 (as in Fig. 10) of the 10 members of the GOOD composite group. Black dashed lines indicate the mean RI-onset time of GOOD.

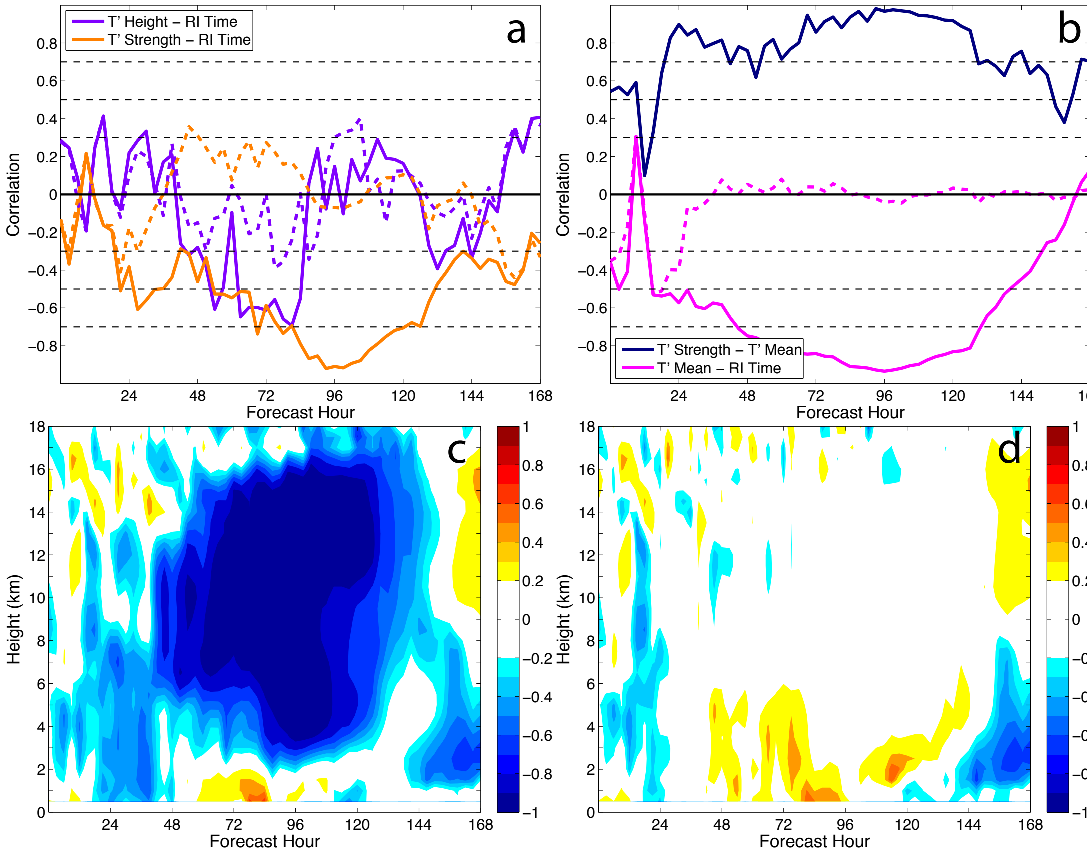

Figure 12. (a) Evolution of the correlation (solid) and part correlation controlling for minimum SLP (dashed) between the RI times of the 30 developing composite group members and both the height (purple) and the strength of the maximum perturbation temperature (orange). (b) As in (a), but for the vertically averaged inner-core (within 25-km of the surface center) perturbation temperature (magenta). Correlation between the vertically averaged inner-core perturbation temperature and the strength of the maximum perturbation temperature is also plotted (dark blue). (c) Time-height correlation between the strength of the maximum perturbation temperature and the RI-onset time of the 30 members of the developing composite groups. (d) As in (c), but for the part correlation controlling for the current intensity (minimum SLP).